

Formation of supermassive stars in the first star clusters

Bastián Reinoso¹★, Ralf S. Klessen^{1,2}, Dominik Schleicher³, Simon C. O. Glover¹, and P. Solar³

¹Universität Heidelberg, Zentrum für Astronomie, Institut für Theoretische Astrophysik, Albert-Ueberle-Str. 2, 69120 Heidelberg, Germany

²Universität Heidelberg, Interdisziplinäres Zentrum für Wissenschaftliches Rechnen, Im Neuenheimer Feld 205, 69120 Heidelberg, Germany

³Departamento de Astronomía, Facultad Ciencias Físicas y Matemáticas, Universidad de Concepción, Av. Esteban Iturra s/n Barrio Universitario, Casilla 160-C, Concepción, Chile

Accepted XXX. Received YYY; in original form ZZZ

ABSTRACT

The formation of supermassive stars is believed to be an essential intermediate step for the formation of the massive black hole seeds that become the supermassive black holes powering the quasars observed in the early Universe. Numerical simulations have shown that supermassive stars can form in atomic-cooling halos when protostars reach accretion rates higher than $\sim 10^{-2} M_{\odot} \text{ yr}^{-1}$ and fragmentation is suppressed on pc scales. It is however still uncertain if a supermassive star still emerges when fragmentation occurs at smaller scales and a cluster of stars is formed instead. In this work we explore the problem of massive object formation due to the interplay of collisions and accretion in star clusters at low metallicity. We model a small embedded cluster of accreting protostars following sub-parsec scale fragmentation during the collapse of a primordial gas cloud and follow its evolution by performing N -body plus hydrodynamical simulations. Our results show that supermassive stars with 10^3 and $10^4 M_{\odot}$ are always formed due to the interplay of collisions and accretion, and in some cases these objects are part of a binary system. The resulting supermassive star is surrounded by tens of smaller stars with typical masses in the range 1–100 M_{\odot} .

Key words: methods: numerical – early Universe – quasars: supermassive black holes – stars: formation – stars: Population III

1 INTRODUCTION

As of today more than 200 quasars have been detected at redshift $z > 5.7$ (Fan et al. 2006; Mortlock et al. 2011; Wu et al. 2015; Bañados et al. 2018; Reed et al. 2019; Onoue et al. 2019; Bañados et al. 2021; Wang et al. 2021), with masses larger than $10^9 M_{\odot}$, and notably, more than $10^{10} M_{\odot}$ for SDSS J010013.02+280225.8 (Wu et al. 2015). Explaining the formation and growth of the supermassive black holes (SMBHs) powering those quasars, at an age of the Universe of less than a billion years, is still an important open problem in astrophysics (see the reviews by Volonteri 2010; Woods et al. 2019). A natural approach to solve this problem is to find and study the processes capable of yielding massive black holes (BHs) early in the history of the Universe. These early-formed massive BHs are the seeds that grow further by accreting matter, continuous mergers, or both; becoming finally the most distant quasars observed today.

The most straightforward path that yields massive BH seeds comes from the death of massive population III stars (Abel et al. 2002; Heger & Woosley 2002; Heger et al. 2003; Klessen 2019), whose initial mass function (IMF) is believed to be top heavy as supported by recent numerical simulations (Stacy et al. 2016; Fraser et al. 2017; Riaz et al. 2018; Sharda et al. 2020). This scenario however faces important limitations as the formed seeds are still too light ($\lesssim 10^2 M_{\odot}$). In addition, because massive Pop III stars are very effective at expelling gas from the low mass halos in which they form, the black holes formed from them are ‘born starving’ in regions of low gas density and thus cannot grow efficiently by gas accretion

(Johnson & Bromm 2007; Smith et al. 2018). An alternative pathway for massive black hole seed formation is the runaway growth of a single star due to stellar collisions in very dense star clusters (Omukai et al. 2008; Katz et al. 2015; Sakurai et al. 2017, 2019; Reinoso et al. 2018, 2020; Vergara et al. 2021), or black hole mergers in dense black hole clusters (Davies et al. 2011; Lupi et al. 2014). This channel yields massive objects with typical masses of $10^3 M_{\odot}$. These BHs could grow to $10^9 M_{\odot}$ by $z \sim 7$ if they accreted continuously at the Eddington limit, but this is an unlikely scenario considering the environment in which those seeds emerge. A recent work by Escala (2021) suggests that a runaway collision process in nuclear star clusters could produce BHs with masses up to $10^9 M_{\odot}$.

The pathway that yields the most massive BH seeds is the so-called direct collapse black hole (DCBH) scenario, and as of today it seems the most plausible explanation for the highest redshift quasars observed. Initially proposed by Rees (1984), this formation channel consists of the accumulation of a huge amount of matter in a sufficiently small volume, following the collapse of a pristine gas cloud. This process yields a supermassive star (SMS) that collapses to a BH due to the post-Newtonian instability (Chandrasekhar 1964).

Stellar structure calculations show that SMSs are inflated objects, with effective temperatures of 10^4 K, that can reach final masses of $10^5 M_{\odot}$ before collapsing due to the post-Newtonian instability (Chandrasekhar 1964; Hosokawa et al. 2012, 2013; Schleicher et al. 2013; Woods et al. 2017; Haemmerlé et al. 2018; Haemmerlé 2021). Given their low effective temperature, they are unable to produce ionizing photons that may terminate accretion due to radiative feedback. Furthermore, considering the gas-rich environments in which those

★ E-mail: bastian.reinoso@uni-heidelberg.de

objects form, they are promising candidates to produce the massive BH seeds that can grow further by mass accretion.

Recent numerical simulations explored the collapse of pristine gas clouds in the early Universe and found that an essential condition for the formation of SMSs in such environments is the suppression of molecular hydrogen cooling, which would otherwise lead to fragmentation of the cloud and the formation of population III stars. Preventing the cooling due to molecular hydrogen requires a decrease of its abundance by photodetachment of the H^- ion and the destruction of the H_2 molecule. This can be achieved in the presence of a strong radiation background that carries photons in the Lyman-Werner bands ($11.2 \text{ eV} \leq h\nu \leq 13.6 \text{ eV}$) and dissociates the H_2 molecule, along with infrared photons ($h\nu \geq 0.76 \text{ eV}$) that lower the abundance of H^- , a catalyst for H_2 formation. This can occur if two pristine halos remain at a small separation such that once star formation begins in one of them, the other is exposed to a high Lyman-Werner radiation intensity, thus suppressing molecular hydrogen cooling. This is termed the ‘synchronized pairs’ scenario (Dijkstra et al. 2008; Visbal et al. 2014; Chon et al. 2018). Once molecular hydrogen cooling has been suppressed, cooling occurs primarily via collisional excitation of hydrogen atoms, provided that the gas temperature is high enough to make this process efficient. Halos in which this is the case are often referred to as atomic-cooling halo.

The radiation intensity needed to suppress molecular hydrogen cooling is usually expressed in units of J_{21} , where $J_{21} = 1$ corresponds to a radiation intensity of $10^{-21} \text{ erg cm}^{-2} \text{ s}^{-1} \text{ sr}^{-1} \text{ Hz}^{-1}$ at the Lyman limit (see e.g. Omukai 2001; Latif et al. 2015). The required radiation intensity on the atomic-cooling halo could be as high as $J_{21} = 1000$ (Regan et al. 2014; Latif et al. 2015) or even higher when considering an X-ray background (Inayoshi & Tanaka 2015; Glover 2016), and the true value has important implications for the number density of DCBHs (Dijkstra et al. 2014; Inayoshi & Tanaka 2015; Chon et al. 2016, 2018).

It has been suggested (Wise et al. 2019) that extremely high radiation intensities are not a necessary condition as long as the dark matter halo grows rapidly through mergers. The dynamical heating induced by this period of rapid growth, combined with a moderate Lyman-Werner flux of $J_{21} \sim 3$ can still produce accretion rates of the order of $0.1\text{--}1 \text{ M}_\odot \text{ yr}^{-1}$ onto the central object. Once the right conditions are met and high accretion rates achieved ($> 0.04 \text{ M}_\odot \text{ yr}^{-1}$), an SMS can still emerge.

The ideal places for the emergence of DCBHs are overdense regions in the early Universe, as they provide intense radiation backgrounds and rapid halo growth. This has been investigated via semi-analytic models by Lupi et al. (2021), suggesting that the ‘synchronized pairs’ channel as well as the dynamically heated halos can produce several BH seeds in these environments.

Although a single object forms initially in idealized scenarios of pristine atomic-cooling halos irradiated by a high intensity LW background, it is important to follow its evolution for longer times in order to place constraints on its final mass. High resolution numerical simulations have shown that fragmentation is unavoidable in the accretion disk for the high accretion rates expected in these environments, and fragmentation is seen on $\sim \text{au}$ scales (Clark et al. 2011; Greif et al. 2012; Latif et al. 2016; Becerra et al. 2018; Suazo et al. 2019; Patrick et al. 2020; Wollenberg et al. 2020; Latif et al. 2021; Jaura et al. 2022; Prole et al. 2022a,b). It is therefore important to understand the fate of the halos that failed to remain metal-free and/or of the ones in which an important degree of fragmentation is expected. This scenario is now being explored, and various models, both numerical and analytical, have shown that SMSs with $10^{4\text{--}5} \text{ M}_\odot$

might still be able to form (Boekholt et al. 2018; Alister Seguel et al. 2020; Tagawa et al. 2020; Das et al. 2021; Schleicher et al. 2022). These results seem to be confirmed by the more sophisticated simulations of Chon & Omukai (2020). Additionally, Sassano et al. (2021) showed that under Eddington-limited accretion, the heavy black hole seeds ($\sim 10^5 \text{ M}_\odot$) are able to produce 10^9 M_\odot BHs at $z \sim 6$ (see also Trinca et al. 2022 for a similar analysis involving light BH seeds).

In this paper we present a set of N -body plus hydrodynamics simulations that include mass accretion, mass-radius parametrizations and stellar mergers to model the central region of a collapsed primordial cloud in which multiple protostars are present. We explore two environments similar to the ones expected in atomic-cooling halos to assess the impact of fragmentation at sub parsec scales during the assembly of DCBHs. We describe our simulation setup in Sec. 2, then present our results in Sec. 3 and a discussion in Sec. 4.

2 SETUP

In this section we describe the initial conditions for our models, the numerical codes used, and additional algorithms that we include in our simulations.

2.1 Initial conditions

The clusters are modelled to consist of a combination of gas and protostars, the former represented by SPH particles and the latter by particles that interact only through gravity, which we also refer to as N -body particles throughout this paper. We model two clusters that differ only in the total mass being 10025.6 in one case and 30025.6 M_\odot in the other. In both cases, we start with a total mass of 25.6 M_\odot in protostars, so the initial gas masses are 10000 and 30000 M_\odot , respectively. The initial number of protostars is 256 and each of them has a mass of 0.1 M_\odot which is consistent with the mass of protostars formed in atomic-cooling halos (Becerra et al. 2015). The gas is sampled with 2^{18} SPH particles. For each set of particles (SPH and protostars), the positions are sampled from a Plummer distribution (Plummer 1911) with a Plummer radius $R_p \sim 0.077 \text{ pc}$ such that the half-mass radius is $R_h \sim 1.3R_p = 0.1 \text{ pc}$ and we impose a cut-off radius of 5 Plummer radii for each model such that all the mass is enclosed within $\sim 0.4 \text{ pc}$. This yields an initial number density for protostars of 956 pc^{-3} . We adopt this distribution for simplicity, as the precise distribution of gas and protostars will be unknown. However, it ensures a meaningful behavior of both quantities in the central region, where the density profile will be flat, while the behaviour in the outer parts will approximately resemble the behaviour found in cosmological simulations (e.g. Latif et al. 2015). The velocities of the protostars are obtained by imposing virial equilibrium condition. We relax the Plummer distribution of SPH particles and then inject a spectrum of non-compressive Kolmogorov turbulence with Mach number $\mathcal{M} = 1$ as found in numerical simulations by Latif et al. (2013).

2.2 Numerical simulations

To run our simulations we use the Astrophysical MULTI-purpose Software Environment (AMUSE¹, see Portegies Zwart et al. 2009, 2013; Pelupessy et al. 2013; Portegies Zwart & McMillan 2018), a

¹ <https://github.com/amusecode/amuse>

PYTHON interface designed to couple existing numerical codes, offering great flexibility and allowing us to relatively easily include new algorithms such as mass accretion onto the protostars, sink particle creation, a treatment for stellar collisions, and mass radius relations for the protostars, all of them described in the next subsections.

2.3 *N*-body-SPH coupling

We couple the pure *N*-body code PH4 (McMillan & Hut 1996) and the SPH code FI (Hernquist & Katz 1989; Gerritsen & Icke 1997; Pelupessy et al. 2004) by means of the BRIDGE method (Fujii et al. 2007) via the *bridge* class included in AMUSE. This method consists of calculating the gravitational acceleration at the position of the *N*-body particles using the SPH particles and vice versa, i.e., the particles in one code kick the particles in the other code. To ensure that the coupling does not violate Newton’s third law, we use the code FastKick to perform the kicks, with a constant gravitational smoothing length of 0.5 au, approximately equal to the smallest smoothing length among all the SPH particles. By doing so we employ the same gravitational smoothing kernel for both sets of particles and make sure that the gravitational forces among them are symmetric.

For evolving the particles in the *N*-body code we use a smoothing length of $1 R_{\odot}$ in order to accurately solve gravitational interactions between the protostars. We include an external pressure floor in the SPH code by modifying the momentum equation in an analogous way as done in Benz (1990); Clark et al. (2011). This external pressure is equal to the pressure of the cloud at the cut-off radius, and corresponds to $\sim 1.72 \times 10^{-7} \text{ g cm}^{-1} \text{ s}^{-2}$ for the most massive cloud and $\sim 7.45 \times 10^{-8} \text{ g cm}^{-1} \text{ s}^{-2}$ for the less massive cloud. The external pressure is required to stabilize the clouds against vacuum boundary conditions.

Finally, we modified the code FI to include a modified equation of state of the form

$$T = T_0 \left[1 + \left(\frac{\rho}{\rho_c} \right)^{\gamma-1} \right], \quad (1)$$

so that the gas behaves isothermally, with a temperature $T_0 = 8000 \text{ K}$ at low densities, but becomes adiabatic at densities above $\rho_c = 10^{15} \text{ cm}^{-3}$, as found in 1D and 3D models including detailed chemical networks (Omukai et al. 2008; Becerra et al. 2015). We use an adiabatic index $\gamma = 5/3$.

The treatment of stellar collisions (described in Sec. 2.9) as well as the mass radius relations are implemented at the PYTHON level. The mass accretion (see Sec. 2.6) and sink particle creation (see Sec. 2.7) algorithms are written in FORTRAN and included as PYTHON functions via F2PY for adequate performance. This offers the advantage of easily replacing any of the codes used without having to re-write these routines.

The time integration consists sequentially of the Kick-Drift-Kick (KDK) integration with *bridge* during which stellar collisions and sink particle creation are solved, followed by the computation of accretion onto the protostars, and the treatment of stellar ejections. We impose a maximum timestep of 5 yr for *bridge* in order to perform the accretion steps rather frequently, given the rapid accretion rates expected in this environment.

The densest gas is typically found around accreting protostars and thus it is often accreted after every accretion step. Nevertheless there are regions where the gas becomes very dense and thus the associated free-fall time can be of the order of 10^{-4} yr . Because of this we implemented an adaptive time-stepping algorithm for *bridge*,

such that the timestep is reduced by factors of 2 until becoming smaller than the shortest free-fall time. The timestep can increase by a factor of 2 after each timestep only if the shortest free-fall time is more than twice the current timestep.

2.4 Protostars and stars

The *N*-body particles in our simulations are meant to represent, in an approximate way, protostars and stars, but they interact here only through gravity and we do not include any type of feedback. By taking advantage of the particle sets provided by AMUSE we assign additional properties to our *N*-body particles such as: *stage* and *luminosity*. The *stage* property indicates if an *N*-body particle has already entered the main sequence phase or if it is still in the protostellar phase. This distinction is important as inflated protostars can still contract to the main-sequence phase and thus will follow different mass-radius relations. A correct determination of the size of the particles is an essential feature needed in this very dense collisional environment. For the determination of the radius of each *N*-body particle we incorporate new PYTHON functions without the need to modify any code. The mass radius parametrization that we use is briefly described in Sec. 2.5 and further details are provided in Appendix A.

2.5 Mass-radius parametrization

We use a parametrization of the mass-radius relation based on the works by Hosokawa & Omukai (2009) and Hosokawa et al. (2012, 2013). This implementation is simplified by the use of the *stage* property for our *N*-body particles. We define three stages in which an *N*-body particle can be. The possible stages are the *protostar*, *star*, and *supermassive star* stages.

For a particle in the *protostar* stage, the mass-radius relation depends on its mass and accretion rate. We present in Fig. 1, with dashed lines, the mass radius relations for protostars accreting at different rates. The implementation is described in Appendix A.

For a particle in the *star* stage, the mass-radius relation is given by:

$$R_* = 0.97 \left(\frac{M_*}{M_{\odot}} \right)^{0.57} R_{\odot}. \quad (2)$$

It is used once the protostars enter in the main-sequence stage, and corresponds to the blue solid line onto which most of the other lines converge in Fig. 1.

An *N*-body particle enters into the *supermassive star* stage if it is still on the *protostar* stage and if its accretion rate becomes larger than a critical accretion rate \dot{M}_{crit} . The mass-radius relation for these particles is given by:

$$R_* = 2600 \left(\frac{M_*}{100 M_{\odot}} \right)^{1/2} R_{\odot}. \quad (3)$$

It is shown with a dot-dashed line in Fig. 1.

We note that an *N*-body particle in the *protostar* stage will eventually contract to the main sequence after becoming massive enough. Similarly, an *N*-body particle in the *supermassive star* stage can also contract to the main sequence if its accretion rate drops below a critical value \dot{M}_{crit} for a time longer than the Kelvin-Helmholtz (KH) timescale t_{KH} . We adopt here $\dot{M}_{\text{crit}} = 0.04 M_{\odot} \text{ yr}^{-1}$ (Hosokawa et al. 2013).

Due to the structure of supermassive stars, the relevant timescale for contraction is the Kelvin-Helmholtz timescale evaluated at the

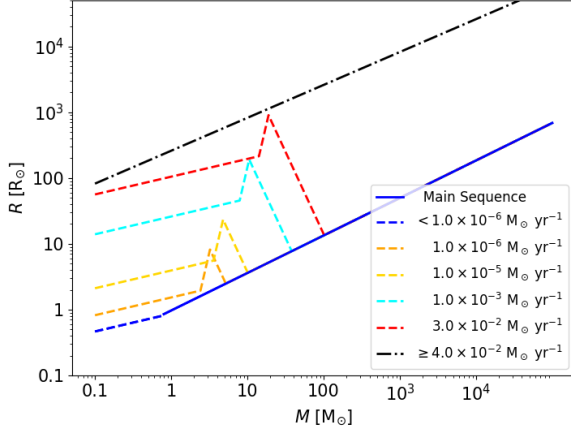


Figure 1. The adopted mass radius relations for accreting protostars in our models.

stellar surface $t_{\text{KH,surf}}$ (Schleicher et al. 2013; Sakurai et al. 2015). The value of the KH timescale at the surface for these objects can be approximated as $10\text{--}100 t_{\text{KH}}$ (Sakurai et al. 2015). We explore here these two extreme values, namely $t_{\text{KH,surf}} = 10 t_{\text{KH}}$ and $100 t_{\text{KH}}$. The first case is the most pessimistic case for stellar collisions to occur whereas the second is the most optimistic case. In consequence, in our simulations, an N -body particle in the *supermassive star* stage will contract if its accretion rate falls below \dot{M}_{crit} for a time longer than $t_{\text{KH,surf}}$ given by:

$$t_{\text{KH,surf}} = X t_{\text{KH}} = X \frac{GM^2}{RL}, \quad (4)$$

with $X = 10$, or $X = 100$.

In order to calculate $t_{\text{KH,surf}}$ we make use of the *luminosity* property of our N -body particles. Luminosities are calculated based on the works by Hosokawa & Omukai (2009) and Hosokawa et al. (2012, 2013) as described in Appendix A.

Finally we also assume that a stellar merger will perturb the new object in such a way that the resulting object has to start over the relaxation process. This means that stellar mergers help to keep the protostars inflated in our simulations.

2.6 Gas accretion

After every KDK step, we calculate the gas accretion onto the protostars. We model the gas accretion by employing the algorithm developed by Hubber et al. (2013). For every N -body particle we define a spherical volume called the interaction zone, with radius $R_{\text{I.Z.}}$. Inside this region the weighted average gas flux onto the central point mass is computed, with the weight calculated via a cubic spline kernel function.

The radius of the interaction zone is adjusted iteratively before every accretion calculation, with a maximum of 50 iterations per particle, to maintain a constant gas mass of $M_{\text{int,max}} = 50 M_{\text{gas}}/N_{\text{SPH}}$ (the mass corresponding to 50 SPH particles). We impose lower and upper limits to the radius of the interaction zone of $r_{\text{min}} = \max(10 \text{ au}, 2R_{\text{star}})$ and $r_{\text{max}} = 500 \text{ au}$, respectively, so that the interaction zone cannot be smaller than the protostars. We also impose the angular momentum conservation condition for the accreted gas and the angular momentum feedback from the point particle as described

in Hubber et al. (2013), as well as the prescriptions for spherical or disk accretion.

Once the accretion step has been completed, we update the radius of each star particle according to the mass-radius parametrization described in Sec. 2.5 and in Appendix A.

2.7 Sink particles

Given the high densities reached in our simulations, we decided to include sink particle creation to avoid prohibitively small timesteps. Based on the work by Hubber et al. (2013), specifically on their ‘NewSink’ algorithm, we create sink particles whenever an SPH particle reaches a density higher than 10^{16} cm^{-3} (Becerra et al. 2015), it sits in a minimum of the gravitational potential among its neighbours, it does not overlap existing sinks, and fulfills the density criterion:

$$\rho_i > \rho_{\text{Hill}} \equiv \frac{3X_{\text{Hill}}(-\Delta\mathbf{r}_{is'} \cdot \Delta\mathbf{a}_{is'})}{4\pi G|\Delta\mathbf{r}_{is'}|^2}, \quad (5)$$

for all existing sinks s' for a given SPH particle i . Here $\Delta\mathbf{r}_{is'}$ and $\Delta\mathbf{a}_{is'}$ are the relative position and acceleration of sink candidate i with respect to existing sink s' . We set $X_{\text{Hill}} = 4$. This Hill sphere criterion ensures that an SPH particle turns into a sink particle in the vicinity of another sink only if the density peak dominates the local gravitational potential. Once the previous conditions are fulfilled, we remove the SPH particle from FI and insert a new N -body particle in PH4. The mass, position, and velocity of the new particle are the same as the ones of the removed SPH particle. The radius of the protostar is initialized to $0.1 R_{\odot}$ but is recalculated after every accretion step according to the mass-radius parametrization described in Section 2.5.

The Jeans mass scales as

$$M_J \propto \left(\frac{T^3}{n}\right)^{1/2}, \quad (6)$$

with n being the number density of the gas. In our simulations the minimum Jeans mass is $\sim 3.96 M_{\odot}$. The mass resolution is equal to twice the mass contained inside the smoothing length of an SPH particle. In our case this is

$$M_{\text{res}} = 2N_{\text{neigh}} \frac{M_{\text{gas}}}{N_{\text{SPH}}}, \quad (7)$$

where $N_{\text{neigh}} = 64$ is the number of neighbours for one SPH particle as adopted in the code FI, M_{gas} is the initial cloud mass, and N_{SPH} is the number of SPH particles.

In order to avoid artificial fragmentation, our simulations need to resolve the Jeans mass (Bate & Burkert 1997). We achieve the mass resolution by using $N_{\text{SPH}} = 1\,048\,576$ for all our simulations.

2.8 Ejections

The N -body particles can also be ejected from the cluster. A particle is considered to have been ejected once it fulfills three criteria: its distance to the centre of mass of the system is $\geq 1.4 \text{ pc}$; its gravitational potential energy plus kinetic energy per unit mass is positive; and it is moving away from the cluster, i.e., $\mathbf{r} \cdot \mathbf{v} > 0$. Ejected particles are removed from the simulation.

2.9 Collisions

A collision between two particles occurs once the radii of two N -body particles overlap during the N -body integration. This is implemented in AMUSE with the help of the *stopping conditions*. We activate the *stopping condition* that detects the overlap of two particle's radii in PH4, i.e., a collision occurs when

$$d \leq R_1 + R_2,$$

where d is the separation between the particles and R_1 and R_2 are their radii. Once the condition is fulfilled, the integration is interrupted, and then, by implementation at the PYTHON level, we replace the overlapping particles by a new particle that is placed at the centre of mass of the previous configuration and the new velocity is calculated assuming linear momentum conservation. We assume no mass loss to occur, and thus the new mass is the sum of the masses of the colliding particles, i.e.

$$M_{\text{new}} = M_1 + M_2.$$

In order to determine the new radius of the merger product, we first determine the stage in which the new particle will be, according to the outcomes shown in Tab. B1; and the new track, in case the resulting stage is *protostar*, is assigned as shown in Table B2. Subsequently the new radius is obtained from the corresponding mass-radius relation. Further details are provided in Appendix B. After determining the evolutionary stage of the particle, the luminosity is calculated as explained in Appendix A.

3 RESULTS

In this section we describe the results obtained from our simulations. We begin by describing the general behaviour of the simulated systems in which we set $t_{\text{KH,surf}} = 100 t_{\text{KH}}$ (see Sec. 2.5). We describe the emergence of massive objects and characterize the final state of the clusters. We do so first for the simulations with $M_{\text{gas}} = 10^4 M_{\odot}$ and then for simulations with $M_{\text{gas}} = 3 \times 10^4 M_{\odot}$. We then show the impact of setting $t_{\text{KH,surf}} = 10 t_{\text{KH}}$ on the final masses of the most massive objects. All the uncertainties reported correspond to the one sigma interval assuming a normal distribution.

3.1 Clusters with $M_{\text{gas}} = 10^4 M_{\odot}$

3.1.1 Cluster evolution

By the time that we stop our simulations, most of the gas accretion has already occurred as depicted in Fig. 2. The initial phase of the evolution is marked by a contraction of the inner parts of the gas cloud on a free-fall timescale. We see the contraction of the inner parts of the cloud, up to the radius at which 25 per cent of the total mass is enclosed, i.e. the 25 per cent Lagrangian radius. This takes place at around 6000 yr and marks the beginning of the short time-span during which most of the gas accretion takes place.

During this contraction, turbulence does not significantly affect the cloud evolution as no substructures appear and we observe a spherical collapse, which in turn causes high accretion rates onto a central object around which a gaseous disk is formed. This object quickly becomes the most massive object (MMO) of the cluster.

By the end of the simulations the total accreted mass reaches typical values of $4612 \pm 798 M_{\odot}$, i.e., $\sim 46 \pm 8$ per cent of the initial mass, and the mean total mass in stars that are still bound to the cluster is $4131 \pm 791 M_{\odot}$. The mean mass in ejected stars is $481 \pm 338 M_{\odot}$.

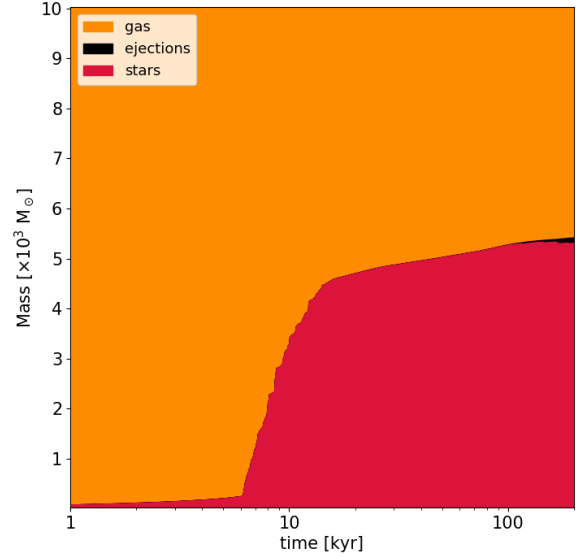


Figure 2. Mass of the gas, bound stars and ejected stars during the evolution of the system for one of our simulations with $M_{\text{gas}} = 10^4 M_{\odot}$ (M1_t100_1).

3.1.2 Emergence of very massive objects

In most of our simulations we see the formation of a single object that contains most of the accreted mass. The typical mass of the MMO is $3729 \pm 792 M_{\odot}$. We define a parameter ϵ to assess the efficiency of the formation of a massive object. It is defined as $\epsilon = M_{\text{MMO}}/M_{\text{gas}}$ and shown for each simulation in Table 1. We find a mean efficiency $\epsilon = 0.37 \pm 0.08$.

We also see that in one third of the simulations, the MMO is in a binary system with another very massive object. We define a pair of bound stars to be in a binary system if they follow a Keplerian orbit and the mass ratio $q = M_1/M_2$ is less than 7. This choice for this mass ratio is arbitrary but allow us to select high mass stars that are in a binary system with the MMO which are the binary systems in which we are interested.

We show the properties of the binary systems in Table 2, and we note that in simulations with a binary system, there are fewer stars in the final stellar system due to more collisions occurring and more ejections due to three body interactions (see columns 11, 12 and 13 in Table 1).

The overall contraction of the gas cloud causes a strong inflow and therefore a high accretion rate onto one of the central protostars. We show the evolution of this object that becomes the MMO in Fig. 3. The maximum accretion rates in the simulations are a few $M_{\odot} \text{ yr}^{-1}$, surpassing during some time the critical accretion rate of $\dot{M}_{\text{crit}} = 0.04 M_{\odot} \text{ yr}^{-1}$, and thus creating an MMO that emerges in the cloud centre and evolves as a supermassive star. This moment can be distinguished in the second panel of Fig. 3 at the point when the solid orange line first crosses the gray dashed line. Because of this the star inflates up to around $2 \times 10^4 R_{\odot}$, i.e., $\sim 93 \text{ au}$ as it now follows the mass-radius relation shown with a black dot-dashed line in Fig. 1. The increased cross section of the central star results in a period of runaway collisions with the MMO. The collision rate reaches a maximum of 0.1 collisions per year just after the MMO has

Table 1. Summary of simulation outcomes. We present for each simulation the initial gas mass, the final time, the quiescent time adopted for contraction to the main sequence for supermassive stars, the simulation outcome, the total accreted mass, the final stellar mass bound to the most massive object, the mass of the most massive object, the efficiency of massive object formation, the total mass in ejected stars, the number of stars bound to the MMO, the number of ejections and the number of collisions.

Simulation	M_{gas} [M_{\odot}]	t_{end} [yr]	$t_{\text{KH,surf}}$ [t_{KH}]	outcome	M_{accreted} [M_{\odot}]	$M_{\text{stellar,bound}}$ [M_{\odot}]	M_{MMO} [M_{\odot}]	ϵ	M_{ejected} [M_{\odot}]	N_{stars}	$N_{\text{ejections}}$	N_{col}
M1_t100_1	10^4	200 015	100	single	5 414	5 305	5 197	0.52	109	56	70	256
M1_t100_2	10^4	200 005	100	single	3 815	3 482	3 311	0.33	333	62	112	288
M1_t100_3	10^4	200 043	100	single	4 709	4 539	3 893	0.39	170	56	77	341
M1_t100_4	10^4	200 023	100	single	3 730	3 315	3 048	0.30	415	48	153	291
M1_t100_5	10^4	200 017	100	binary	5 854	4 821	4 096	0.41	1 033	6	141	369
M1_t100_6	10^4	200 050	100	binary	4 150	3 326	2 831	0.28	824	15	196	300
M1_t10_1	10^4	200 024	10	single	5 397	4 952	4 326	0.43	445	66	83	343
M1_t10_2	10^4	120 045	10	single	4 548	4 377	4 156	0.42	171	88	79	375
M1_t10_3	10^4	200 022	10	binary	6 057	5 297	4 064	0.41	760	65	147	364
M1_t10_4	10^4	200 029	10	binary	5 262	4 468	2 901	0.29	794	86	141	456
M1_t10_5	10^4	200 036	10	single	6 804	6 256	4 858	0.49	548	89	53	412
M1_t10_6	10^4	112 701	10	single	4 617	4 255	4 135	0.41	362	56	119	301
M3_t100_1	3×10^4	200 021	100	single	26 108	25 808	24 418	0.81	300	13	42	1 892
M3_t100_2	3×10^4	200 043	100	single	26 939	26 898	26 890	0.90	41	10	19	1 842
M3_t100_3	3×10^4	200 009	100	single	26 388	26 211	24 577	0.82	177	11	34	2 547
M3_t100_4	3×10^4	200 038	100	single	23 312	22 850	20 365	0.68	462	36	53	1 844
M3_t100_5	3×10^4	200 034	100	single	23 070	22 973	22 618	0.75	97	12	50	2 215
M3_t100_6	3×10^4	200 035	100	single	26 966	26 851	24 375	0.81	115	3	29	2 522
M3_t10_1	3×10^4	200 008	10	single	20 981	20 831	20 435	0.68	150	13	70	2 283
M3_t10_2	3×10^4	200 026	10	single	23 451	23 063	20 776	0.69	388	32	61	1 807
M3_t10_3	3×10^4	200 048	10	single	25 871	25 413	22 267	0.74	458	6	50	2 354
M3_t10_4	3×10^4	200 014	10	single	22 585	21 889	21 733	0.72	696	10	89	2 445
M3_t10_5	3×10^4	200 039	10	single	20 778	20 481	20 368	0.68	297	6	96	2 297
M3_t10_6	3×10^4	200 011	10	single	27 051	26 846	26 746	0.89	205	7	42	3 514

inflated in radius, but starts to decline as the number of protostars decreases, as shown in the middle panel of Fig. 4. The mass accretion rate due to collisions can reach very high values of up to $2 M_{\odot} \text{ yr}^{-1}$.

Additionally we see that huge gas densities ($\rho \sim 10^{-8} \text{ g cm}^{-3}$) around the MMO trigger the formation of ~ 217 new sink particles on average. Almost all (95.4 ± 1.7 per cent) of these new sinks merge with other objects, but only 34 ± 7 per cent of them merge with the MMO. We show the mass distribution of the particles that merge with the MMO in Fig. 5.

Despite the accretion rate falling below the critical accretion rate \dot{M}_{crit} , the frequent stellar collisions prevent the contraction of the MMO. We note that the mass contributed by collisions to this object is around 60 per cent of its final mass as shown in Fig. 6.

3.1.3 Final cluster properties

The typical outcome of our simulations is a small cluster of stars with almost no gas left. This final stellar cluster in most simulations is made up of ~ 50 stars with typical masses in the range $1\text{--}10 M_{\odot}$ surrounding the MMO. No more significant gas accretion is taking place at 200 kyr, and we would expect radiative feedback from the stars to efficiently evaporate the remaining gas. The final mass functions are similar in shape as well as the number of remaining and ejected stars, although a few clusters contain a binary system and fewer stars remain bound due to the increased number of collisions and three body interactions effectively ejecting lower mass objects.

We present the combined mass distribution at the end of simula-

Table 2. Properties of binary systems. We present the mass of the most and less massive object M_1 and M_2 respectively, the semi-major axis a and the eccentricity e .

Simulation	M_1 [M_{\odot}]	M_2 [M_{\odot}]	a [au]	e
M1_t100_5	4 096	688	355	0.126
M1_t100_6	2 831	464	240	0.375
M1_t10_3	4 064	831	472	0.394
M1_t10_4	2 901	1 224	120	0.077

tions M1_t100_1–6 in Fig. 7, and the combined mass distribution of ejected particles in Fig. 8. Individual mass distributions of bound and ejected particles for each simulation are presented in Figs. D1 and D2.

3.2 Clusters with $M_{\text{gas}} = 3 \times 10^4 M_{\odot}$

In this section we describe the general evolution of the clusters with $3 \times 10^4 M_{\odot}$ in gas, and mention the differences with the less massive clusters.

3.2.1 Cluster evolution

The initial behaviour of the gas cloud is the same for all the simulations, and also very similar to the behaviour in the less massive clusters. We see that most of the gas is accreted early on in the cloud

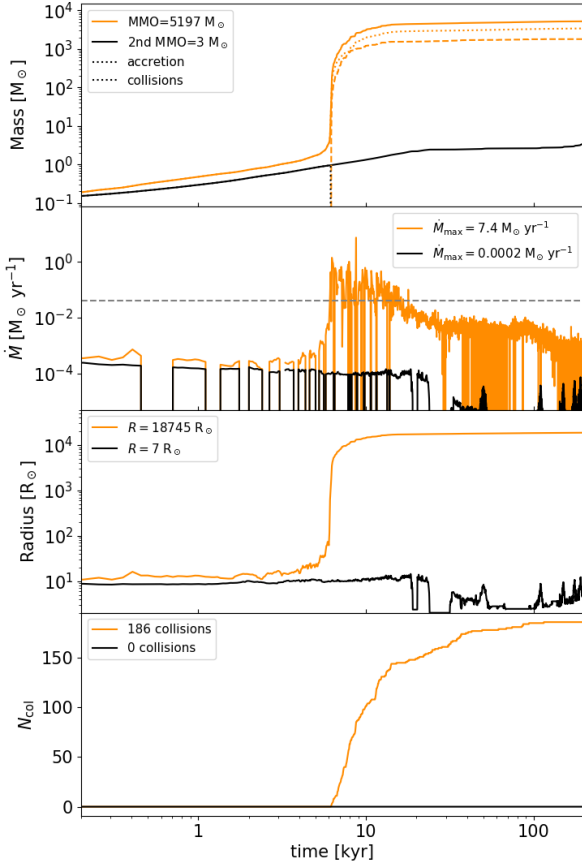


Figure 3. Evolution of the mass M , accretion rate \dot{M} and radius R for the MMO and second MMO in one of our simulations (M1_t100_2), along with the number of collisions N_{col} as functions of time.

evolution as depicted in Fig. 9. During the initial evolution the inner parts of the cloud experience an overall contraction. Specifically, we see a contraction of the 25 per cent Lagrangian radius, which leads to a rapid inflow of gas to the central parts of the cluster in a free-fall time, i.e., ~ 3000 yr. Unlike in the less massive clusters, we also see a contraction at the 50 per cent Lagrangian radius.

Turbulence seems to have a negligible role here as no substructure appears during the initial contraction and a spherical collapse proceeds. During the rapid mass inflow either a central object starts to accrete most of the mass, or a new sink particle is created at the centre due to the high gas densities. This central particle reaches accretion rates of several $10 M_{\odot} \text{ yr}^{-1}$, and the average efficiency $\epsilon = 0.80 \pm 0.07$ means that this single object gathers on average 80 ± 7 per cent of the total mass of the cloud.

3.2.2 Emergence of very massive objects

In all our simulations with $M_{\text{gas}} = 3 \times 10^4 M_{\odot}$ we see the formation of a single object that contains on average 80 ± 7 per cent of the initial cluster mass at 200 kyr. This means that the average mass

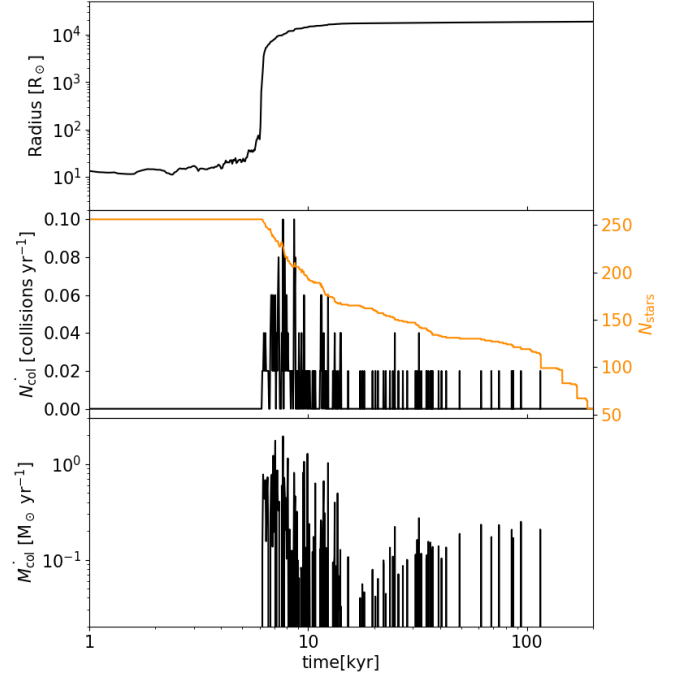


Figure 4. Radius of the MMO, collision rate along with the number of protostars, and mass accretion rate due to collisions as functions of time for one of our simulations (M1_t100_1).

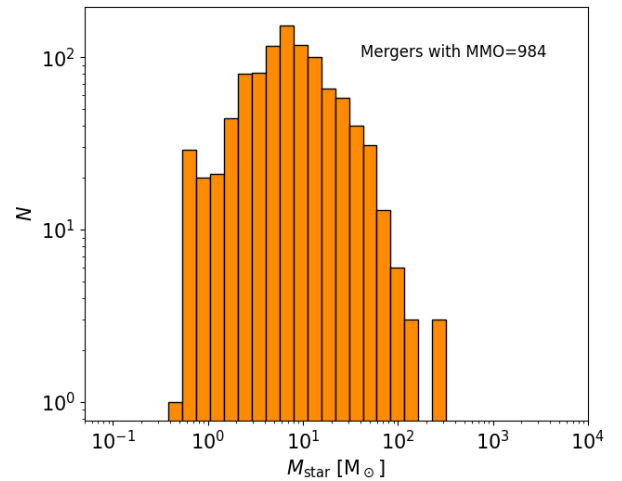


Figure 5. Mass distribution of the particles that merge with the MMO for simulation M1_t100_1–6.

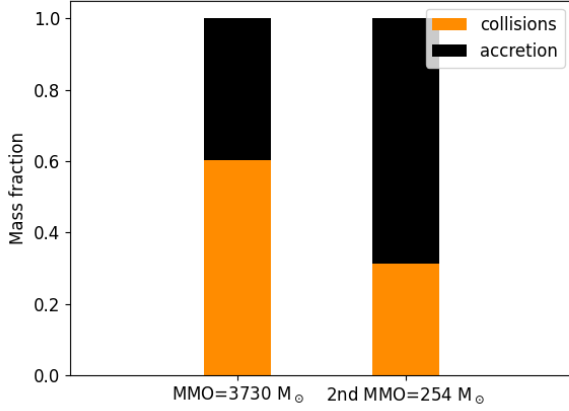


Figure 6. Average mass fraction gained through collisions and accretion, and average masses for the MMO and second MMO for simulations M1_t100_1–6.

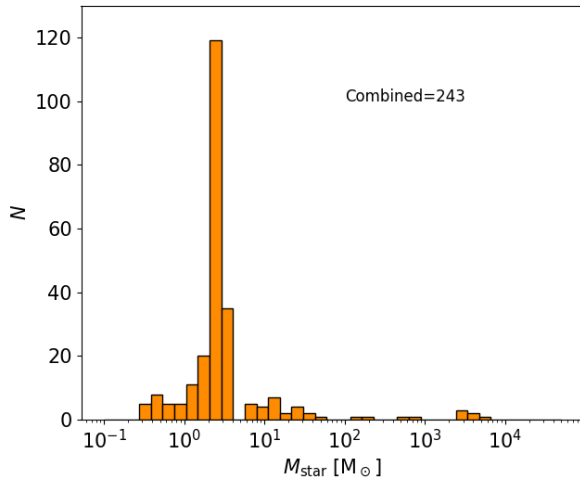


Figure 7. Combined mass distribution for stars bound to the cluster at the end of simulations M1_t100_1–6.

of the MMO is $23873 \pm 2001 M_{\odot}$. We present in Fig. 10 some of the properties of the MMO, like the mass, accretion rate, radius, and number of collisions it experiences during the evolution of the system. This particle also evolves as a supermassive star due to the high accretion rates that it reaches, and grows both by accretion of gas and stellar collisions. The mass growth by mergers with other protostars contributes on average 46 per cent of its final mass as shown in Fig. 11. Unlike in the less massive clusters, here higher accretion rates are reached, and they last for longer. We also see that stellar collisions contribute with a smaller mass fraction to the final mass of the MMO. This is simply due to the fact that in the simulations with $M_{\text{gas}} = 3 \times 10^4 M_{\odot}$, the MMO gains much more mass by gas accretion.

Gas accretion peaks on average at $10 M_{\odot} \text{ yr}^{-1}$ and remains above the critical accretion rate during the initial 8 000 yr after the initial cloud contraction. This is sufficient to cause the protostar to evolve as

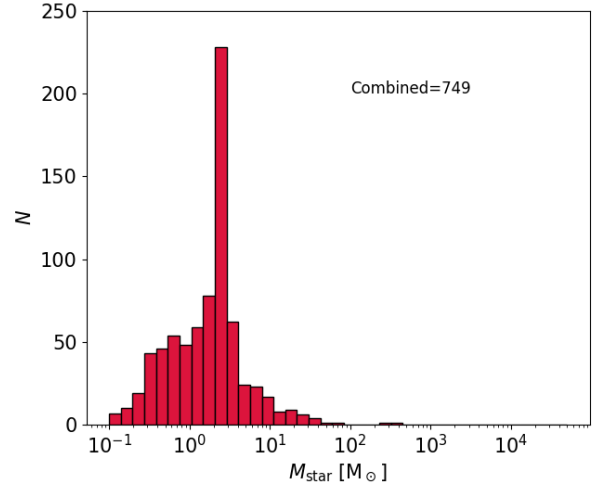


Figure 8. Combined mass distribution of ejected stars at the end of simulations M1_t100_1–6.

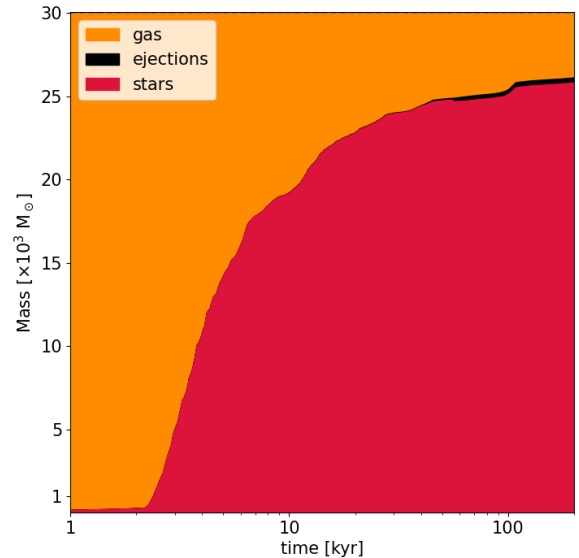


Figure 9. Same as Fig. 2 but for a cluster with $M_{\text{gas}} = 3 \times 10^4 M_{\odot}$.

an inflated object that quickly reaches a radius of more than 100 au, which in turn causes many stellar collisions to occur. We see in Fig. 12 that the collision rate peaks just after the MMO inflates in radius, reaching a peak of more than 0.3 collisions per year, a factor 3 higher than for the lower mass cloud simulations. The mass accretion due to collisions reaches peaks of $\sim 10 M_{\odot} \text{ yr}^{-1}$, a factor 10 higher than for the less massive cloud simulations. The collision rate then decreases with the number of protostars.

Additionally, the huge gas densities ($\rho \sim 10^{-8} \text{ g cm}^{-3}$) found around the MMO trigger the formation of sink particles, 1 950 new sink particles on average. Nearly all of these sink particles ($\sim 99 \pm 0.2$ per cent) merge with other objects, notably, 70 ± 5 per cent of the

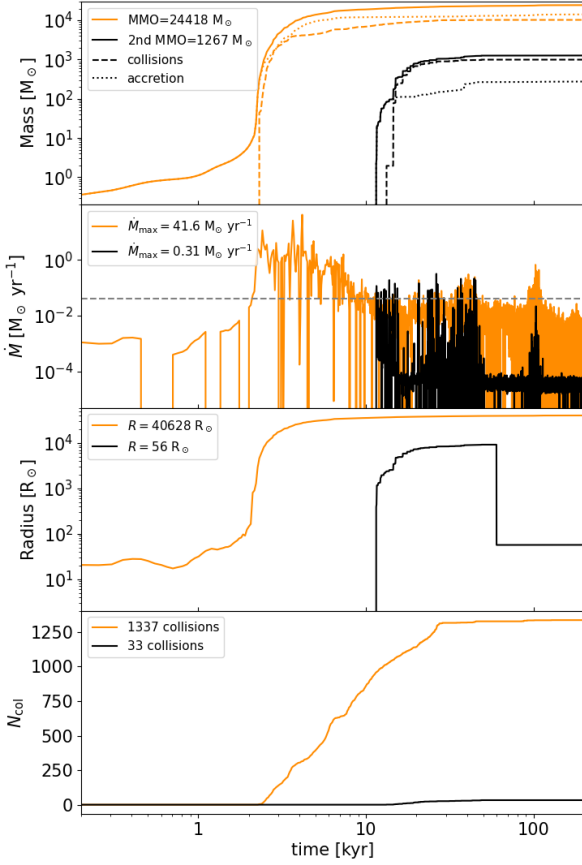


Figure 10. Same as Fig. 3 but for a cluster with $M_{\text{gas}} = 3 \times 10^4 M_{\odot}$.

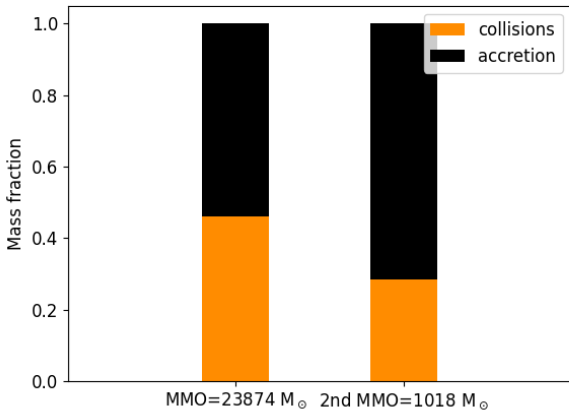


Figure 11. Average mass fractions gained through collisions and accretion, and average final masses for the MMO and the second MMO for simulations M3_t100_1–6.

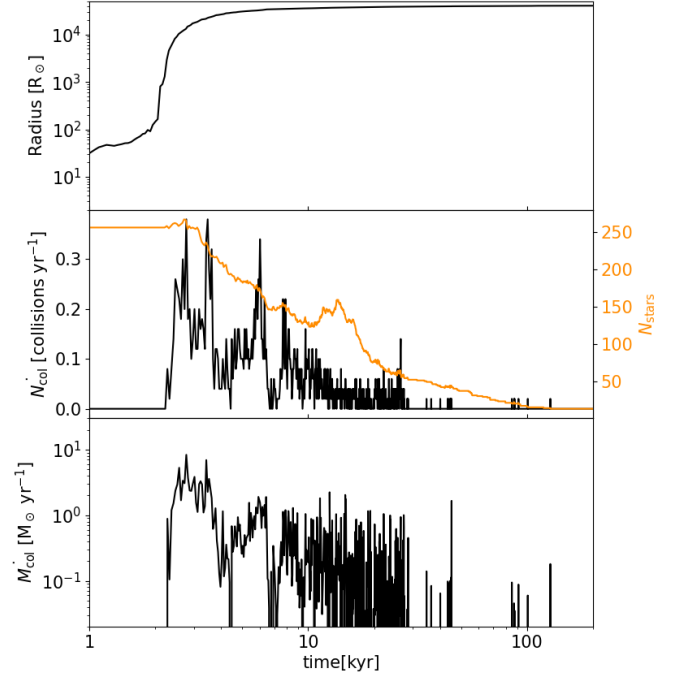


Figure 12. Same as Fig. 4 but for a cluster with $M_{\text{gas}} = 3 \times 10^4 M_{\odot}$.

sinks merge with the MMO, and most of them do so shortly after they are created when they have accreted only 1–2 M_{\odot} . Sink particles in this mass range that merge with the MMO represent 52 ± 9 per cent of the total number of mergers, but they contribute on average only 11 ± 4 per cent of the total mass gained through mergers. We show the mass distribution of the sink particles that merge with the MMO in Fig. 13.

3.2.3 Final cluster properties

At the end of our simulations the remaining stellar systems consist of, on average, only 14 ± 10 particles with an average of 38 ± 12 ejected ones. Little to no gas is left and the final cluster is essentially comprised of an MMO with $\sim 2 \times 10^4 M_{\odot}$ that is orbited by a few other stars, most of them with masses in the range 1–10 M_{\odot} . In 3 simulations, the second most massive object reaches more than 1000 M_{\odot} and is orbiting the MMO in a close Keplerian orbit, but since the mass ratio $q = M_1/M_2$ is too high (> 20), we do not mark them as binary systems.

We show the combined mass distribution of the particles that remain bound to the MMO for simulations M3_t100_1–6 in Fig. 14. Comparing this mass distribution to the mass distribution of less massive clusters shown in Fig. 7, the immediate difference that we note is that now we do not have a prominent peak. Instead the mass distribution looks flat in the mass range 1–100 M_{\odot} .

We also show the combined mass distribution of ejected particles for these simulations in Fig. 15. This looks more similar to the one for less massive clusters, but with an additional peak at $\sim 0.1 M_{\odot}$. While the shape of the mass function is maintained it now peaks in between 1–2 M_{\odot} instead of 2–3 M_{\odot} as observed for less massive

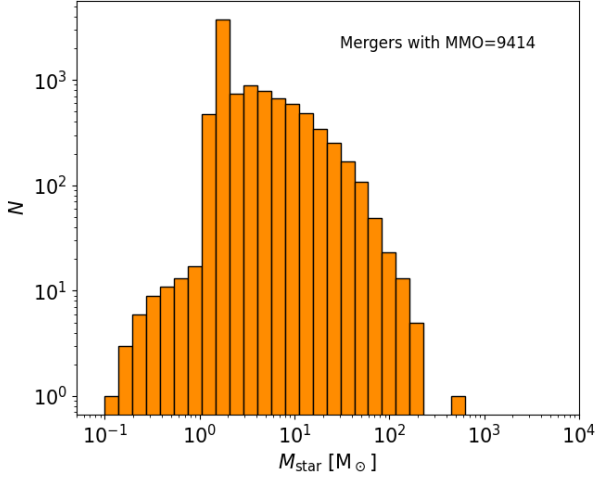


Figure 13. Mass distribution of the particles that merge with the MMO for simulation M3_t100_1.

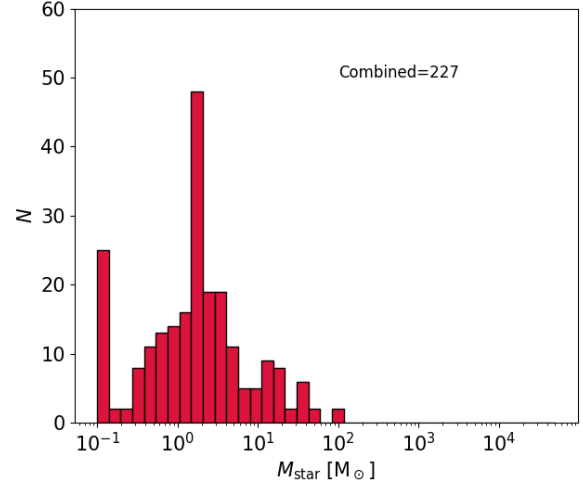


Figure 15. Combined mass distribution for stars ejected from the cluster at the end of simulations M3_t100_1-6.

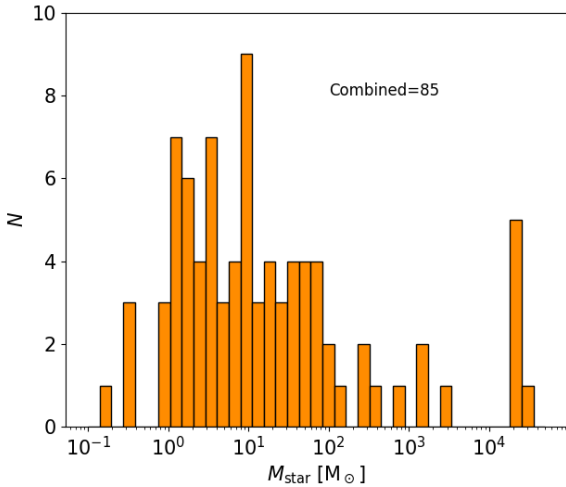


Figure 14. Combined mass distribution for stars bound to the cluster at the end of simulations M3_t100_1-6.

clusters.

We present the individual mass distribution of bound and ejected particles for each of these simulations in Figs. D3 and D4, respectively.

3.3 Impact of a reduced $t_{\text{KH,surf}}$

As explained at the end of Sec. 2.5 the time it takes for an inflated SMS to contract to the main sequence after its accretion rate falls below \dot{M}_{cirt} (i.e. $t_{\text{KH,surf}}$) ranges in between 10–100 t_{KH} (Sakurai et al. 2015). So far we have assumed $t_{\text{KH,surf}} = 100 t_{\text{KH}}$ and found that the MMOs in our simulations reach an average mass of 3 729 M_{\odot} for clusters with $M_{\text{gas}} = 10^4 M_{\odot}$ and 23 873 M_{\odot} for clusters with $M_{\text{gas}} = 3 \times 10^4 M_{\odot}$.

In principle a shorter $t_{\text{KH,surf}}$ would cause an earlier contraction to the main sequence and this could impact the formation of an MMO via two effects. The first one is related to the growth via stellar collisions. An earlier contraction to the main sequence implies that the protostars that evolve as SMSs will not maintain a high cross-section for long enough times compared to simulations with $t_{\text{KH,surf}} = 100 t_{\text{KH}}$. The second effect is a reduction of the mass of the stars that evolve as SMSs, given that gas accretion should terminate once the star contracts to the main sequence. Because of this, the simulations with $t_{\text{KH,surf}} = 10 t_{\text{KH}}$ would have the highest impact on the final mass of the MMO.

In order to explore the effects of a reduced $t_{\text{KH,surf}}$ on the final masses of the MMOs we ran simulations with $t_{\text{KH,surf}} = 10 t_{\text{KH}}$ for our two different cluster models (see Table 1) and compare the results to the ones from our simulations with $t_{\text{KH,surf}} = 100 t_{\text{KH}}$. This gives us an idea of how much a reduced $t_{\text{KH,surf}}$ would impact the formation of an MMO through stellar collisions. Then in order to get an idea of how our results would change when including radiation feedback we post process the snapshots of our simulations with $t_{\text{KH,surf}} = 10 t_{\text{KH}}$. For this we stop the mass growth of all particles once they contract to the main sequence and use the existing merger history, but now with the modified masses to obtain a new estimate for the final mass of the MMO.

3.3.1 Clusters with $M_{\text{gas}} = 10^4 M_{\odot}$

For the set of simulations with $M_{\text{gas}} = 10^4 M_{\odot}$ (M1_t100_1–6 and M1_t10_1–6), by comparing the final masses of the MMOs (column 7) we find that the average values are consistent within one sigma errors. In fact, for simulations with $t_{\text{KH,surf}} = 100 t_{\text{KH}}$, the average mass of the MMO is $\sim 3\,700 \pm 800$, whereas for simulations with $t_{\text{KH,surf}} = 10 t_{\text{KH}}$, the average mass of the MMO is $\sim 4\,000 \pm 600$. Therefore we find that an earlier contraction to the main sequence has no impact on the growth of the MMO via stellar collisions and that the different values that we find here are the result of the intrinsic variability among different simulations.

The MMO does not contract to the main sequence but this is not due to very frequent stellar collisions, the mean time between collisions

(~ 2700 yr) is actually slightly longer than $10 t_{\text{KH}}$ (~ 1700 yr). We attribute this behaviour to very short accretion bursts that surpass \dot{M}_{crit} during a brief period of time (< 50 yr) not captured in Fig. 3 since the cadence for data output is 50 yr.

Subsequently, after including an approximate effect of feedback (i.e., stopping the mass growth of a star once it enters the main sequence) we find very little reduction of the stellar masses. For simulations with $t_{\text{KH,surf}} = 10 t_{\text{KH}}$ the average final mass of the MMO goes down to $\sim 3800 \pm 500 M_{\odot}$ after post-processing. This is still within the one sigma error of the value obtained without any type of feedback. We show the comparison of the final masses of the MMOs in the case without feedback and in the case with approximate feedback in the left panel of Fig. 16.

Finally, we also note that the same holds true for the binary systems formed in these simulations. We find a reduction of only 10 per cent for the masses of the primary and secondary stars, and the mass ratios remain the same.

3.3.2 Clusters with $M_{\text{gas}} = 3 \times 10^4 M_{\odot}$

We first compare the final mass of the MMO for simulations with $t_{\text{KH,surf}} = 100 t_{\text{KH}}$ and $t_{\text{KH,surf}} = 10 t_{\text{KH}}$. For the first case the average mass of the MMO is $\sim 23800 \pm 2000 M_{\odot}$, and for the second case the average mass of the MMO is $\sim 22000 \pm 2200 M_{\odot}$. Thus we find again that an earlier contraction to the main sequence will not reduce the final mass of the MMO due to collisions appreciably. The MMO still remains inflated due to frequent mergers and this is the main driver of stellar collisions. The different values that we find here are a result of the intrinsic simulation to simulation variation.

When we post-process our simulations to account for the approximate effect of radiation feedback we find that the average mass of the MMO is reduced to $\sim 21500 \pm 2200 M_{\odot}$ which again is within the one sigma error of the average mass of the MMO when no feedback is considered. We thus conclude that radiation feedback would not appreciably reduce the mass of the MMO. We show the final average masses of the MMOs when no feedback is included and with approximate feedback in the right panel of Fig. 16.

We find however that the mass of the second most massive object is severely affected. On average the post-processing reduces the mass of the second MMO by a factor of four, and in one case even a factor of six. This occurs because in the simulations where a higher density is reached in the cloud centre, many protostars initially evolve as SMSs as they surpass the critical accretion rate. They however cannot maintain the high accretion rates for long times and eventually contract to the main sequence. In the simulations with high $t_{\text{KH,surf}}$ this timespan of lower accretion rates is not long enough for the stars to contract to the main sequence, but in post-processing when $t_{\text{KH,surf}}$ is lower they contract and their masses are fixed at that point.

3.3.3 Possible impact of feedback from surrounding stars

Regarding the formation and growth of the MMO we try to understand if once another protostar close to the MMO contracts to the main sequence, it would appreciably impact the final mass of the MMO. For this purpose we calculate the Strömgren radius of the first star that enters the main sequence in our simulations and that is close enough to influence the growth of the MMO. We find that the first

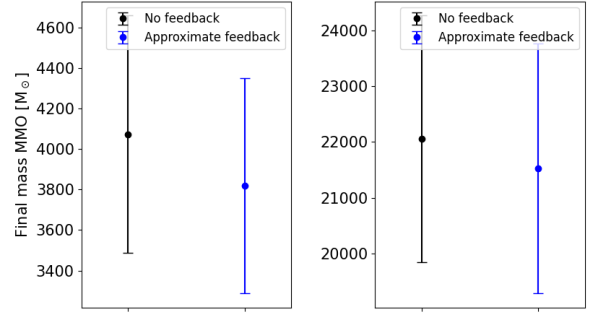


Figure 16. Estimate for the approximate effects of radiation feedback on the final mass of the MMO obtained from post-processing of our simulations. *Left panel:* Average final mass of the MMO with one sigma errorbars for simulations with $M_{\text{gas}} = 10^4 M_{\odot}$ and $t_{\text{KH,surf}} = 10 t_{\text{KH}}$. *Right panel:* Same as left panel but for simulations with $M_{\text{gas}} = 3 \times 10^4 M_{\odot}$ and $t_{\text{KH,surf}} = 10 t_{\text{KH}}$.

star enters the main sequence once the MMO has already gathered more than 80 per cent of its final mass, and the typical separation between these objects is around 500 au, but the Strömgren radius for the main sequence star (as calculated in Appendix C) is usually around 6 au. Therefore we conclude that the surrounding stars that enter the main sequence will not appreciably impact the final mass of the MMO, which can also still grow through stellar mergers.

4 DISCUSSION AND CONCLUSIONS

In this work we address the problem of massive object formation, considering the evolution of a protostellar cluster embedded in a massive gas cloud at very low metallicity following fragmentation at sub-parsec scales, during the collapse of an atomic-cooling halo. We perform a suite of hydrodynamical plus N -body simulations including sink particle creation, gas accretion, pseudo (proto-)stellar evolution and stellar collisions. Our calculations start from a Plummer distribution of protostars embedded in a gas cloud that follows a Plummer density profile as well, and to which we impose a turbulent velocity field with Mach number equal to one, resembling the centre of a spherically collapsing atomic-cooling halo as found in cosmological hydrodynamical simulations (Chon et al. 2018). We note that spherical collapse is not always the case, and elongated clouds are also found in these simulations, so it will be desirable to begin with initial conditions taken directly from cosmological simulations in the future. Despite this, no fragmentation at parsec-scales is seen during these simulations, and we expect that fragmentation at smaller scales, as studied here, will not impede the formation of a supermassive star with $10^4 M_{\odot}$.

Our simulations include (proto-)stellar evolution in the sense that the stellar radius and luminosity change with the mass and accretion rate of the protostar. Therefore the protostars are allowed to contract to the main sequence and thus reduce the cross-section for collisions. This is essential because survival, ejection, and merger rates depend sensitively on the object size. One caveat in our simulations comes from the fact that we do not include stellar feedback. We estimate the possible impact of radiation feedback on the final mass of the MMO in Sec. 3.3. For this purpose we post-processed our simulations and stop mass accretion once the object enters the main sequence, at which point we assume that strong UV radiation may remove gas

from the surrounding. In this extreme model, further mass growth is only possible via collisions. We find that this modification has negligible impact on the final masses of the MMO, and similar holds for the binary systems when present. We also calculate the Strömgren radius of surrounding stars that enter the main sequence but find that they do so once the MMO has already gathered more than 80 per cent of its final mass and these stars are not close enough to affect the growth of the MMO. We find however that the masses of the second most massive object could be affected in simulations with $M_{\text{gas}} = 3 \times 10^4 M_{\odot}$. This indicates that in order to fully characterize the final stellar masses in such systems, simulations that include radiation feedback are required.

The simulation results presented here agree with the study by [Chon & Omukai \(2020\)](#) where they find what they termed a ‘super-competitive accretion’ in which a single massive object dominates the growth by gas accretion. The conditions under which this scenario emerges were recently studied by means of analytical arguments by [Schleicher et al. \(2023\)](#). They demonstrate that self-gravity induced accretion will initially dominate the mass growth of an object that will become the most massive object in the cluster and this does not depend on the number of protostars present. Only after the gas accretion mode shifts from self-gravity to Bondi-Hoyle, due to lower gas densities, could the fragments around the MMO interfere with gas accretion onto it, however, the moment at which this occurs depends only on the square root of the number of protostars. We conclude that in the context of atomic cooling halos as studied here, in an initially Jeans-unstable cloud, varying the initial number of protostars will have little to no impact on the mass growth through accretion.

We note that we model systems with a high initial number density of protostars (see Sec. 2.1). We tried to estimate the effect that a lower initial number density of protostars would have on the final mass of the MMOs. For this purpose we consider the extreme scenario in which no initial protostars are present and post-process the collision histories to remove all the mass contributed by these protostars to the MMO. In this extreme scenario in which that mass would be lost from the system we find that for our simulations with $10^4 M_{\odot}$ in gas, the mass of the MMO decreases by 36 per cent; and in our simulations with $3 \times 10^4 M_{\odot}$ in gas, the mass is reduced by 11 per cent. This reduction in mass would still leave MMOs that can collapse to produce massive black holes seeds.

Since we consider protostars forming in a pristine gas cloud, the stars that are formed in our simulations resemble primordial stars, in particular the so-called Population III stars. These stars, once on the main sequence, do not lose significant mass due to stellar winds because of their low metallicity ([Krtićka & Kubát 2006](#)), therefore including mass loss due to stellar winds will not change our results.

Moreover, the MMOs formed in our simulations evolve as super-massive stars because of the high accretion rate they reach ([Schleicher et al. 2013](#); [Hosokawa et al. 2013](#); [Haemmerlé et al. 2018](#); [Haemmerlé 2021](#)). Again, due to their low metallicity, no mass loss is expected from stellar winds. Furthermore [Hosokawa et al. \(2013\)](#) demonstrated that mass loss due to the pulsational instability reaches a maximum of $\sim 5 \times 10^{-3} M_{\odot} \text{ yr}^{-1}$, much lower than the accretion rates that these objects experience. It is thus safe to also ignore mass loss for our MMOs. Note that mass loss due to stellar winds is relevant for higher metallicity stars when considering the formation of massive objects due to stellar collisions as explored in the context of nuclear star clusters by [Das et al. \(2021\)](#).

Finally, we note that the sink particles we consider resemble protostars but eventually some of them reach the zero age main sequence (ZAMS) and turn into stars. The point at which this typically occurs is around 30 kyr when protostars accreting at high rates reach the Kelvin–Helmholtz contraction phase ([Hosokawa & Omukai 2009](#)). At this moment the MMO has gathered more than 80 per cent of its final mass. The typical mass for stars that reach the ZAMS is around $20 M_{\odot}$. Stellar evolution models for these type of stars show main sequence lifetimes in the order of Myr even for very massive stars ([Tanikawa et al. 2020](#); [Murphy et al. 2021](#)), therefore no supernova explosion can occur during the time-span of our simulations.

We have not considered mass loss during stellar collisions. This effect has been studied in the context of blue straggler formation ([Sills & Bailyn 1999](#); [Sills et al. 2000](#)), and in the context of local star clusters. For this purpose, fitting functions depending on the mass ratio of the collision ([Lombardi et al. 2002](#)) and the stellar structure ([Glebbeek et al. 2008](#); [Glebbeek & Pols 2008](#)) have been obtained for stars colliding at different stages during their evolution ([Glebbeek et al. 2013](#)). Armed with these functions [Alister Seguel et al. \(2020\)](#) found that including mass loss could reduce the mass of the MMO by 20–40 per cent in a similar environment to the one studied here. Applied to our simulations, we conclude that the run-away formation of the MMO cannot be prevented. However, we note that it is not clear how well these analytical estimates can be applied to the collision between an SMS and its surrounding stars. More work is required to reduce the uncertainty in these estimates.

The formation of very massive objects that can collapse to produce massive black hole seeds has also been investigated in the context of star cluster formation in non-primordial clouds ([Sakurai et al. 2017, 2019](#); [Das et al. 2021](#)). In these models different mass-radius relations are used as the accretion rates experienced in these environments are much lower. In particular in these studies the stars never evolve as the inflated SMSs produced in our simulations. This lead to important differences in the masses of the objects formed and the timescales involved. Even in presence of a much larger gas reservoir ($10^5 M_{\odot}$) the most massive objects reach typical masses of $10^3 M_{\odot}$ ([Sakurai et al. 2019](#); [Das et al. 2021](#)).

According to previous simulations investigating the formation of SMSs in atomic cooling halos, mass inflows of $0.5 M_{\odot} \text{ yr}^{-1}$ are reported at scales similar to the ones simulated here ([Wise et al. 2019](#)). At this constant rate the flow can be maintained for about 1 Myr which is comparable to the lifetime of the most massive stars formed in our simulations. Assuming that a total of $10^6 M_{\odot}$ have concentrated in the inner 1 pc of the DM halo we estimate a binding energy of $\sim 5 \times 10^{52} \text{ erg}$. On the other hand the binding energy of a $150 M_{\odot}$ Population III star (a typical massive star formed in our simulations) is around $1.7 \times 10^{52} \text{ erg}$. These estimates yield similar quantities, therefore it is very uncertain to say that a supernova explosion will or not be able to eject the remaining gas, it is important to know how much mass is concentrated inside which volume and the final masses of the stars. If the gas is not ejected after the supernova explosion, another episode of star formation could occur in the halo but this time producing second generation stars due to the metal enrichment of the ejecta.

In our simulations we find that a massive central object is always formed and experiences run-away growth via collisions with other protostars in the cluster. The mass growth is typically dominated by one single object as found in previous studies ([Latif et al. 2013](#);

Inayoshi & Haiman 2014; Sakurai et al. 2016; Matsukoba et al. 2019; Chon & Omukai 2020) and explained by analytical arguments by Schleicher et al. (2023). Additionally the fragmentation process does not fully suppress the high mass flow towards the centre and so the MMO continues to grow via gas accretion as well. The MMO begins to grow once the cloud collapses on a free-fall timescale (around 3 000 yr) and by 10 000 yr it already contains 37 per cent of the initial gas mass for clusters with $M_{\text{gas}} = 10^4 M_{\odot}$, and 80 per cent of the initial gas mass for clusters with $M_{\text{gas}} = 3 \times 10^4 M_{\odot}$. 50 to 60 per cent of the mass of the MMO is gained through collisions. In a third of the simulations with $M_{\text{gas}} = 10^4 M_{\odot}$ we find that the MMO is in a binary system with another massive object with mass ratios in between 1:2 and 1:7. Radiation feedback is unable to reduce the mass of the MMO significantly. The final outcome is therefore a small group of tens of stars with typical masses in the range 1–100 M_{\odot} orbiting a single object with 10^3 or $10^4 M_{\odot}$. In one third of the cases the group of stars orbits a pair of massive objects ($\sim 10^3 M_{\odot}$) in a binary configuration.

ACKNOWLEDGEMENTS

BR acknowledges support through ANID (CONICYT-PFCHA/Doctorado acuerdo bilateral DAAD/62180013) as well as support from DAAD (funding program number 57451854). PS acknowledges support through ANID/Doctorado en el Extranjero convocatoria 2022 (funding number 72220198). The team acknowledges funding from the European Research Council via the ERC Synergy Grant “ECOGAL” (project ID 855130), from the Deutsche Forschungsgemeinschaft (DFG) via the Collaborative Research Center “The Milky Way System” (SFB 881 – funding ID 138713538 – subprojects A1, B1, B2 and B8) and from the Heidelberg Cluster of Excellence (EXC 2181 - 390900948) “STRUCTURES”, funded by the German Excellence Strategy. We also thank the German Ministry for Economic Affairs and Climate Action for funding in the project “MAINN” (funding ID 50002206). DRGS gratefully acknowledges support by the ANID BASAL projects ACE210002 and FB210003, via the Millenium Nucleus NCN19-058 (TITANs) and via Fondecyt Regular (project code 1201280). Part of the simulations presented in this work were performed with resources provided by the Kultrun Astronomy Hybrid Cluster via the projects Conicyt Programa de Astronomia Fondo Quimal 2017 QUIMAL170001, Conicyt PIA ACT172033, and Fondecyt Iniciacion 11170268. Most of the simulations were performed on the Helix cluster and BwUniCluster2.0 supported by the state of Baden-Württemberg through bwHPC and the German Research Foundation (DFG) through grant INST 35/1597-1 FUGG, data are stored at SDS@hd funded through grant INST 35/1314-1 FUGG.

DATA AVAILABILITY

The data underlying this article will be shared on reasonable request to the corresponding author.

REFERENCES

Abel T., Bryan G. L., Norman M. L., 2002, *Science*, **295**, 93
 Alister Seguel P. J., Schleicher D. R. G., Boekholt T. C. N., Fellhauer M., Klessen R. S., 2020, *MNRAS*, **493**, 2352
 Bañados E., et al., 2018, *Nature*, **553**, 473

Bañados E., et al., 2021, *ApJ*, **909**, 80
 Bate M. R., Burkert A., 1997, *MNRAS*, **288**, 1060
 Becerra F., Greif T. H., Springel V., Hernquist L. E., 2015, *MNRAS*, **446**, 2380
 Becerra F., Marinacci F., Bromm V., Hernquist L. E., 2018, *MNRAS*, **480**, 5029
 Benz W., 1990, in Buchler J. R., ed., *Numerical Modelling of Nonlinear Stellar Pulsations Problems and Prospects*. p. 269
 Boekholt T. C. N., Schleicher D. R. G., Fellhauer M., Klessen R. S., Reinoso B., Stutz A. M., Haemmerlé L., 2018, *MNRAS*, **476**, 366
 Chandrasekhar S., 1964, *ApJ*, **140**, 417
 Chon S., Omukai K., 2020, *MNRAS*, **494**, 2851
 Chon S., Hirano S., Hosokawa T., Yoshida N., 2016, *ApJ*, **832**, 134
 Chon S., Hosokawa T., Yoshida N., 2018, *MNRAS*, **475**, 4104
 Clark P. C., Glover S. C. O., Smith R. J., Greif T. H., Klessen R. S., Bromm V., 2011, *Science*, **331**, 1040
 Das A., Schleicher D. R. G., Leigh N. W. C., Boekholt T. C. N., 2021, *MNRAS*, **503**, 1051
 Davies M. B., Miller M. C., Bellovary J. M., 2011, *ApJ*, **740**, L42
 Dijkstra M., Haiman Z., Mesinger A., Wyithe J. S. B., 2008, *MNRAS*, **391**, 1961
 Dijkstra M., Ferrara A., Mesinger A., 2014, *MNRAS*, **442**, 2036
 Escala A., 2021, *ApJ*, **908**, 57
 Fan X., et al., 2006, *AJ*, **131**, 1203
 Fraser M., Casey A. R., Gilmore G., Heger A., Chan C., 2017, *MNRAS*, **468**, 418
 Fujii M., Iwasawa M., Funato Y., Makino J., 2007, *PASJ*, **59**, 1095
 Gerritsen J. P. E., Icke V., 1997, *A&A*, **325**, 972
 Glebbeek E., Pols O. R., 2008, *A&A*, **488**, 1017
 Glebbeek E., Pols O. R., Hurley J. R., 2008, *A&A*, **488**, 1007
 Glebbeek E., Gaburov E., Portegies Zwart S., Pols O. R., 2013, *MNRAS*, **434**, 3497
 Glover S. C. O., 2016, arXiv e-prints, [p. arXiv:1610.05679](https://arxiv.org/abs/1610.05679)
 Greif T. H., Bromm V., Clark P. C., Glover S. C. O., Smith R. J., Klessen R. S., Yoshida N., Springel V., 2012, *MNRAS*, **424**, 399
 Haemmerlé L., 2021, *A&A*, **647**, A83
 Haemmerlé L., Woods T. E., Klessen R. S., Heger A., Whalen D. J., 2018, *MNRAS*, **474**, 2757
 Heger A., Woosley S. E., 2002, *ApJ*, **567**, 532
 Heger A., Fryer C. L., Woosley S. E., Langer N., Hartmann D. H., 2003, *ApJ*, **591**, 288
 Hernquist L., Katz N., 1989, *ApJS*, **70**, 419
 Hosokawa T., Omukai K., 2009, *ApJ*, **703**, 1810
 Hosokawa T., Omukai K., Yorke H. W., 2012, *ApJ*, **756**, 93
 Hosokawa T., Yorke H. W., Inayoshi K., Omukai K., Yoshida N., 2013, *ApJ*, **778**, 178
 Hubber D. A., Walch S., Whitworth A. P., 2013, *MNRAS*, **430**, 3261
 Inayoshi K., Haiman Z., 2014, *MNRAS*, **445**, 1549
 Inayoshi K., Tanaka T. L., 2015, *MNRAS*, **450**, 4350
 Jaura O., Glover S. C. O., Wollenberg K. M. J., Klessen R. S., Geen S., Haemmerlé L., 2022, *MNRAS*, **512**, 116
 Johnson J. L., Bromm V., 2007, *MNRAS*, **374**, 1557
 Katz H., Sijacki D., Haehnelt M. G., 2015, *MNRAS*, **451**, 2352
 Klessen R., 2019, *Formation of the first stars*. pp 67–97, [doi:10.1142/9789813227958_0004](https://doi.org/10.1142/9789813227958_0004)
 Krtićka J., Kubát J., 2006, *A&A*, **446**, 1039
 Latif M. A., Schleicher D. R. G., Schmidt W., Niemeyer J., 2013, *MNRAS*, **433**, 1607
 Latif M. A., Bovino S., Grassi T., Schleicher D. R. G., Spaans M., 2015, *MNRAS*, **446**, 3163
 Latif M. A., Schleicher D. R. G., Hartwig T., 2016, *MNRAS*, **458**, 233
 Latif M. A., Khochfar S., Schleicher D., Whalen D. J., 2021, *MNRAS*, **508**, 1756
 Lombardi James C. J., Warren J. S., Rasio F. A., Sills A., Warren A. R., 2002, *ApJ*, **568**, 939
 Lupi A., Colpi M., Devecchi B., Galanti G., Volonteri M., 2014, *MNRAS*, **442**, 3616
 Lupi A., Haiman Z., Volonteri M., 2021, *MNRAS*, **503**, 5046

Matsukoba R., Takahashi S. Z., Sugimura K., Omukai K., 2019, *MNRAS*, **484**, 2605

McMillan S. L. W., Hut P., 1996, *ApJ*, **467**, 348

Mortlock D. J., et al., 2011, *Nature*, **474**, 616

Murphy L. J., et al., 2021, *MNRAS*, **501**, 2745

Omukai K., 2001, *ApJ*, **546**, 635

Omukai K., Schneider R., Haiman Z., 2008, *ApJ*, **686**, 801

Onoue M., et al., 2019, *ApJ*, **880**, 77

Patrick S. J., Whalen D. J., Elford J. S., Latif M. A., 2020, arXiv e-prints, p. arXiv:2012.11612

Pelupessy F. I., van der Werf P. P., Icke V., 2004, *A&A*, **422**, 55

Pelupessy F. I., van Elteren A., de Vries N., McMillan S. L. W., Drost N., Portegies Zwart S. F., 2013, *A&A*, **557**, A84

Plummer H. C., 1911, *MNRAS*, **71**, 460

Portegies Zwart S., McMillan S., 2018, *Astrophysical Recipes; The art of AMUSE*, doi:10.1088/978-0-7503-1320-9.

Portegies Zwart S., et al., 2009, *New Astron.*, **14**, 369

Portegies Zwart S., McMillan S. L. W., van Elteren E., Pelupessy I., de Vries N., 2013, *Computer Physics Communications*, **184**, 456

Prole L. R., Clark P. C., Klessen R. S., Glover S. C. O., 2022a, *MNRAS*, **510**, 4019

Prole L. R., Clark P. C., Klessen R. S., Glover S. C. O., Pakmor R., 2022b, *MNRAS*, **516**, 2223

Reed S. L., et al., 2019, *MNRAS*, **487**, 1874

Rees M. J., 1984, *ARA&A*, **22**, 471

Regan J. A., Johansson P. H., Wise J. H., 2014, *ApJ*, **795**, 137

Reinosa B., Schleicher D. R. G., Fellhauer M., Klessen R. S., Boekholt T. C. N., 2018, *A&A*, **614**, A14

Reinosa B., Schleicher D. R. G., Fellhauer M., Leigh N. W. C., Klessen R. S., 2020, *A&A*, **639**, A92

Riaz R., Bovino S., Vanaverbeke S., Schleicher D. R. G., 2018, *MNRAS*, **479**, 667

Sakurai Y., Hosokawa T., Yoshida N., Yorke H. W., 2015, *MNRAS*, **452**, 755

Sakurai Y., Vorobyov E. I., Hosokawa T., Yoshida N., Omukai K., Yorke H. W., 2016, *MNRAS*, **459**, 1137

Sakurai Y., Yoshida N., Fujii M. S., Hirano S., 2017, *MNRAS*, **472**, 1677

Sakurai Y., Yoshida N., Fujii M. S., 2019, *MNRAS*, **484**, 4665

Sassano F., Schneider R., Valiante R., Inayoshi K., Chon S., Omukai K., Mayer L., Capelo P. R., 2021, *MNRAS*, **506**, 613

Schleicher D. R. G., Palla F., Ferrara A., Galli D., Latif M., 2013, *A&A*, **558**, A59

Schleicher D. R. G., et al., 2022, *MNRAS*, **512**, 6192

Schleicher D. R. G., Reinosa B., Klessen R. S., 2023, *MNRAS*, submitted

Sharda P., Federrath C., Krumholz M. R., 2020, *MNRAS*, **497**, 336

Sills A., Bailyn C. D., 1999, *ApJ*, **513**, 428

Sills A., Bailyn C. D., Edmonds P. D., Gilliland R. L., 2000, *ApJ*, **535**, 298

Smith B. D., Regan J. A., Downes T. P., Norman M. L., O'Shea B. W., Wise J. H., 2018, *MNRAS*, **480**, 3762

Stacy A., Bromm V., Lee A. T., 2016, *MNRAS*, **462**, 1307

Suazo M., Prieto J., Escala A., Schleicher D. R. G., 2019, *ApJ*, **885**, 127

Tagawa H., Haiman Z., Kocsis B., 2020, *ApJ*, **892**, 36

Tanikawa A., Yoshida T., Kinugawa T., Takahashi K., Umeda H., 2020, *MNRAS*, **495**, 4170

Trinca A., Schneider R., Valiante R., Graziani L., Zappacosta L., Shankar F., 2022, *MNRAS*, **511**, 616

Vergara M. Z. C., Schleicher D. R. G., Boekholt T. C. N., Reinosa B., Fellhauer M., Klessen R. S., Leigh N. W. C., 2021, *A&A*, **649**, A160

Visbal E., Haiman Z., Bryan G. L., 2014, *MNRAS*, **445**, 1056

Volonteri M., 2010, *A&ARv*, **18**, 279

Wang F., et al., 2021, *ApJ*, **907**, L1

Wise J. H., Regan J. A., O'Shea B. W., Norman M. L., Downes T. P., Xu H., 2019, *Nature*, **566**, 85

Wollenberg K. M. J., Glover S. C. O., Clark P. C., Klessen R. S., 2020, *MNRAS*, **494**, 1871

Woods T. E., Heger A., Whalen D. J., Haemmerlé L., Klessen R. S., 2017, *ApJ*, **842**, L6

Woods T. E., et al., 2019, *Publications of the Astronomical Society of Australia*, **36**, e027

Wu X.-B., et al., 2015, *Nature*, **518**, 512

APPENDIX A: MASS RADIUS PARAMETRIZATION

We use different mass-radius (M-R) relations depending on the accretion rate of the protostar and on its evolutionary stage. We also calculate associated quantities such as the luminosity and the Kelvin-Helmholtz (KH) timescale. All these properties are calculated after every accretion step. We define three evolutionary stages, namely *protostar*, *star*, and *supermassive star*. The M-R relations for each stage are described below.

A1 Protostar

Every particle in our simulations begins in the *protostar* stage. The M-R parametrizations that we use for them are based on the works of Hosokawa & Omukai (2009) and Hosokawa et al. (2012, 2013). We calculate the properties of each *protostar* by classifying them into three different tracks. The classification depends on the accretion rate \dot{M} . We therefore have the ‘SMS’ track, ‘VMS’ track and ‘NORMAL’ track. Each track is described in the next subsections.

A1.1 ‘SMS’ track

There is a critical accretion rate above which the accreting protostars remain inflated and their radii always increase with the mass. A *protostar* whose accretion rate is higher than this critical accretion rate is in the ‘SMS’ track. The critical accretion rate in our simulations is set to $\dot{M}_{\text{crit}} = 0.04 M_{\odot} \text{ yr}^{-1}$ taken from Hosokawa et al. (2013). For every *protostar* in the ‘SMS’ track, the radius is computed as:

$$R_* = 2600 \left(\frac{M_*}{100 M_{\odot}} \right)^{1/2} R_{\odot}. \quad (\text{A1})$$

The *protostar* will follow this relation unless the accretion rate \dot{M} remains below \dot{M}_{crit} for more than 10–100 t_{KH} (Sakurai et al. 2015; Schleicher et al. 2013), where the KH timescale t_{KH} is calculated as:

$$t_{\text{KH}} = \frac{GM^2}{RL}, \quad (\text{A2})$$

with M , R , and L , being the mass, radius and luminosity of the *protostar*. For the calculation of the KH timescale we need the luminosity of the *protostar*. As long as the mass is $\leq 10 M_{\odot}$ the luminosity is calculated as (Hosokawa & Omukai 2009):

$$L_* = 0.6 \left(\frac{M_*}{M_{\odot}} \right)^{11/2} \left(\frac{R_*}{R_{\odot}} \right)^{-1/2} L_{\odot}, \quad (\text{A3})$$

whereas for $M_* > 10 M_{\odot}$, the luminosity is given by:

$$L_* = 10 \left(\frac{M_*}{M_{\odot}} \right)^3 L_{\odot}, \quad (\text{A4})$$

and for $M_* > 70 M_{\odot}$, the luminosity approaches the Eddington limit and is calculated as:

$$L_* = 3.8 \times 10^6 \left(\frac{M_*}{100 M_{\odot}} \right) L_{\odot}. \quad (\text{A5})$$

Finally, once the *protostar* reaches a mass of $600 M_{\odot}$, it enters the *supermassive star* stage. In case the accretion rate \dot{M} of a *protostar* in the ‘SMS’ track remains below \dot{M}_{crit} for more than a 10–100 KH timescales, the *protostar* will enter a new evolutionary track according to its last value for \dot{M} . We note that the time during which

a protostar in the ‘SMS’ track remains inflated after its accretion rate falls below \dot{M}_{crit} can vary between 10–100 KH timescales (Sakurai et al. 2015). We consider both extreme values for the KH timescales in this work.

A1.2 ‘VMS’ track

Every *protostar* whose accretion rate is in the range $[10^{-6}, 0.04] \text{ M}_{\odot} \text{ yr}^{-1}$ is in the ‘VMS’ track. In this track we distinguish three phases, the *adiabatic accretion phase*, the *swelling*, and the *Kelvin Helmholtz contraction* as described in Hosokawa & Omukai (2009). The *adiabatic accretion phase* holds as long as the mass of the *protostar* is $\leq M_{\text{ad}}$ which is given by:

$$M_{\text{ad}} = 0.9 \left[\left(\frac{\dot{M}}{4.2 \times 10^{-8} \text{ M}_{\odot} \text{ yr}^{-1}} \right) \left(\frac{\dot{M}}{10^{-3} \text{ M}_{\odot} \text{ yr}^{-1}} \right)^{(-0.41/2)} \right]^{(2/9.27)} \text{ M}_{\odot}. \quad (\text{A6})$$

In this phase the luminosity is calculated from Eq.(A3) and the radius as:

$$R_* = 26 \left(\frac{M_*}{\text{M}_{\odot}} \right)^{0.27} \left(\frac{\dot{M}}{10^{-3} \text{ M}_{\odot} \text{ yr}^{-1}} \right)^{0.41} \text{ R}_{\odot}. \quad (\text{A7})$$

Now it is useful to define two parameters α and β :

$$\alpha = 26 \left(\frac{M_{\text{ad}}}{\text{M}_{\odot}} \right)^{-4.73} \left(\frac{\dot{M}}{10^{-3} \text{ M}_{\odot} \text{ yr}^{-1}} \right)^{0.41}, \quad (\text{A8})$$

$$\beta = \alpha \left(1.2 \frac{M_{\text{ad}}}{\text{M}_{\odot}} \right)^{7.5}. \quad (\text{A9})$$

The *swelling* phase holds for *protostars* whose mass is in the range $[M_{\text{ad}}, 1.2M_{\text{ad}}]$. In this phase the luminosity is given by Eq.(A3) and the radius as:

$$R_* = \alpha \left(\frac{M_*}{\text{M}_{\odot}} \right)^5 \text{ R}_{\odot}. \quad (\text{A10})$$

The *Kelvin Helmholtz contraction* phase holds for *protostars* whose mass is in the range $[1.2M_{\text{ad}}, M_{\text{ms}}]$, with M_{ms} given by:

$$M_{\text{ms}} = \left(\frac{\beta}{0.97} \right)^{1/3.07}. \quad (\text{A11})$$

The luminosity in this phase is given by Eq.(A4) and the radius by:

$$R_* = \beta \left(\frac{M_*}{\text{M}_{\odot}} \right)^{-2.5} \text{ R}_{\odot}. \quad (\text{A12})$$

If the mass of a *protostar* in the ‘VMS’ track is larger than M_{ms} , it enters the *star* stage, i.e., it contracts to the main sequence. In case the accretion rate \dot{M} of a *protostar* in the ‘VMS’ track remains below $10^{-6} \text{ M}_{\odot} \text{ yr}^{-1}$ for more than a KH timescale, the *protostar* will enter the ‘NORMAL’ track.

A1.3 ‘NORMAL’ track

The *protostars* whose accretion rate is $\dot{M} < 10^{-6} \text{ M}_{\odot} \text{ yr}^{-1}$ are in the ‘NORMAL’ evolutionary track. As long as their mass is $< 0.8 \text{ M}_{\odot}$, the luminosity is given by Eq.(A3) and their radius is given by:

$$R_* = 0.86 \left(\frac{M_*}{\text{M}_{\odot}} \right)^{0.27} \text{ R}_{\odot}. \quad (\text{A13})$$

If the mass is $\geq 0.8 \text{ M}_{\odot}$ the *protostar* enters the *star* stage.

As long as a particle is in the *protostar* stage, it can move between the three tracks described above. There is a hierarchy for the tracks, with the ‘SMS’ track having the highest hierarchy and the ‘NORMAL’ track having the lowest hierarchy. A *protostar* can move to a track with higher hierarchy if the accretion rate \dot{M} is high enough, but it will only move to a lower hierarchy track if the accretion rate \dot{M} remains lower than the critical accretion rate for the current track during a time longer than a KH timescale.

A2 Star

When a particle is in the *star* stage, the radius and luminosity are those for a star in the main sequence. Therefore the luminosity is given by Eq.(A5) and the radius is calculated as:

$$R_* = 0.97 \left(\frac{M_*}{\text{M}_{\odot}} \right)^{0.57} \text{ R}_{\odot}. \quad (\text{A14})$$

We assume that a particle in the *star* stage will not inflate in radius even if the accretion rate is $\dot{M} \geq 0.04 \text{ M}_{\odot} \text{ yr}^{-1}$, therefore once a star particle has entered the *star* stage, it will always follow the same M-R relation.

A3 Supermassive star

When a particle is in the *supermassive star* stage, the luminosity is given by Eq.(A5) and the radius is given by Eq.(A1). It is worth noting that even after a star particle has entered the *supermassive star* stage, it can still contract if the accretion rate falls below the critical accretion rate for more than 10–100 KH timescales. If that occurs, then the star particle will enter the *star* stage and will follow the mass radius relation given by Eq. A14.

APPENDIX B: PROPERTIES OF THE MERGER PRODUCT

In our simulations the star particles have not only mass and radius, but also an interaction zone radius, angular momentum, an evolutionary stage, and track (see Appendix A). We describe here the method that we follow to determine the new properties for the merger product.

We make the assumption that the mass is conserved and the mass of the merger product is the sum of the masses of the progenitors. We do the same for the angular momentum. For the radius of the interaction zone we select the largest value among the two progenitors.

B1 Stage

Determining the stage of the merger product is important to decide the new radius. Given that particles can be in three different stages, we have six combinations for the merging particles as presented in Table B1.

B2 Track

When the stage of the merger product is decided to be a *protostar*, there are six possibilities for the *track* in which it can be, as shown in Table B2.

If the merging particles happen to be in the *protostar* and *star* stage, then the track of the merger product is simply the track of the *protostar*.

For deciding the radius of the merger product we need to determine the accretion rate. We do this by assigning the highest accretion rate

Table B1. Determination of the evolutionary stage for a merger product

progenitor's stage	<i>protostar</i>	<i>star</i>	<i>supermassive star</i>
<i>protostar</i>	<i>protostar</i>	<i>protostar</i>	<i>supermassive star</i>
<i>star</i>	-	<i>star</i>	<i>supermassive star</i>
<i>supermassive star</i>	-	-	<i>supermassive star</i>

Table B2. Determination of the evolution track for a merger product in the *protostar* stage

progenitor's track	NORMAL	VMS	SMS
NORMAL	NORMAL	VMS	SMS
VMS	-	VMS	SMS
SMS	-	-	SMS

among the progenitors to the merger product. Once the stage, the track, and the accretion rate of the merger product have been decided, the radius is calculated as described in Sec. A, and a new luminosity and KH timescale are also computed.

APPENDIX C: STRÖMGREN RADIUS CALCULATION

In order to provide an estimate for the impact of the stars that contract to the main sequence during the cluster evolution, we provide our calculations of the Strömgren radius at the moment when a star enters the main sequence for the first time in one of our simulations, specifically simulation M1_t100_1.

The Strömgren radius is given by

$$R_s = \left(\frac{3}{4\pi} \frac{Q_\star}{n_H^2 \beta_2(T)} \right)^{1/3}, \quad (\text{C1})$$

where Q_\star is the number of hydrogen ionizing photons ($h\nu \geq 13.6$ eV) per unit time, n_H is the hydrogen nuclei number density and $\beta_2(T)$ is the case B volume recombination rate for hydrogen, which is $\sim 2 \times 10^{-13} \text{ cm}^{-3} \text{ s}^{-1}$ at 10^4 K. We adopt this value here.

The number of ionizing photons can be estimated by using Planck's function as

$$Q_\star = \int_{\nu_1}^{\infty} \frac{L_\nu}{h\nu} d\nu = \frac{8\pi^2 R^2}{c^2} \int_{\nu_1}^{\infty} \frac{\nu^2}{e^{\frac{h\nu}{kT}} - 1} d\nu, \quad (\text{C2})$$

where $h\nu_1 = 13.6$ eV and R is the radius of the star. Now, in this specific simulation the masses of the first star that enters the MS is around $7.5 M_\odot$, this implies a radius of $R \sim 3 R_\odot$, luminosity of $\sim 285363 L_\odot$, and $T_{\text{eff}} \sim 76316$ K. With these values we obtain $\frac{h\nu_1}{kT} \sim 2.1$, so we can approximate the integral in eq.(C2) as

$$\begin{aligned} \int_{\nu_1}^{\infty} \frac{\nu^2}{e^{\frac{h\nu}{kT}} - 1} d\nu &\sim \int_{\nu_1}^{\infty} \frac{\nu^2}{e^{\frac{h\nu}{kT}}} d\nu = \left(\frac{kT}{h} \right)^3 \int_{x_1}^{\infty} \frac{x^2}{e^x} dx \\ &= \left(\frac{kT}{h} \right)^3 (x_1^2 + 2x_1 + 2)e^{-x}, \end{aligned} \quad (\text{C3})$$

where $x = \frac{h\nu}{kT}$.

By doing so, we obtain

$$Q_\star = \frac{8\pi^2 R^2}{c^2} \left(\frac{kT}{h} \right)^3 \left[\left(\frac{h\nu_1}{kT} \right)^2 + 2 \frac{h\nu_1}{kT} + 2 \right] e^{-\left(\frac{h\nu_1}{kT} \right)}. \quad (\text{C4})$$

Inserting the numerical values we obtain

$$Q_\star \sim 2 \times 10^{49} \text{ s}^{-1}. \quad (\text{C5})$$

For estimating the number density of hydrogen atoms, we take the mean density inside a sphere with radius 200 au, centered on the radiation source, and obtain $n_H = 5.6 \times 10^9 \text{ cm}^{-3}$, so the Strömgren radius is

$$R_s = 6 \text{ au}. \quad (\text{C6})$$

We note that the separation between this star and the accreting MMO is 734 au at this moment, thus this star would be unable to stop further accretion onto the MMO.

APPENDIX D: MASS DISTRIBUTIONS

In this appendix we present the mass distribution of bound and ejected stars, at the end of, and for each of our simulations with $t_{\text{KH,surf}} = 100 t_{\text{KH}}$.

D1 Clusters with $M_{\text{gas}} = 10^4 M_\odot$

D2 Clusters with $M_{\text{gas}} = 3 \times 10^4 M_\odot$

This paper has been typeset from a \LaTeX file prepared by the author.

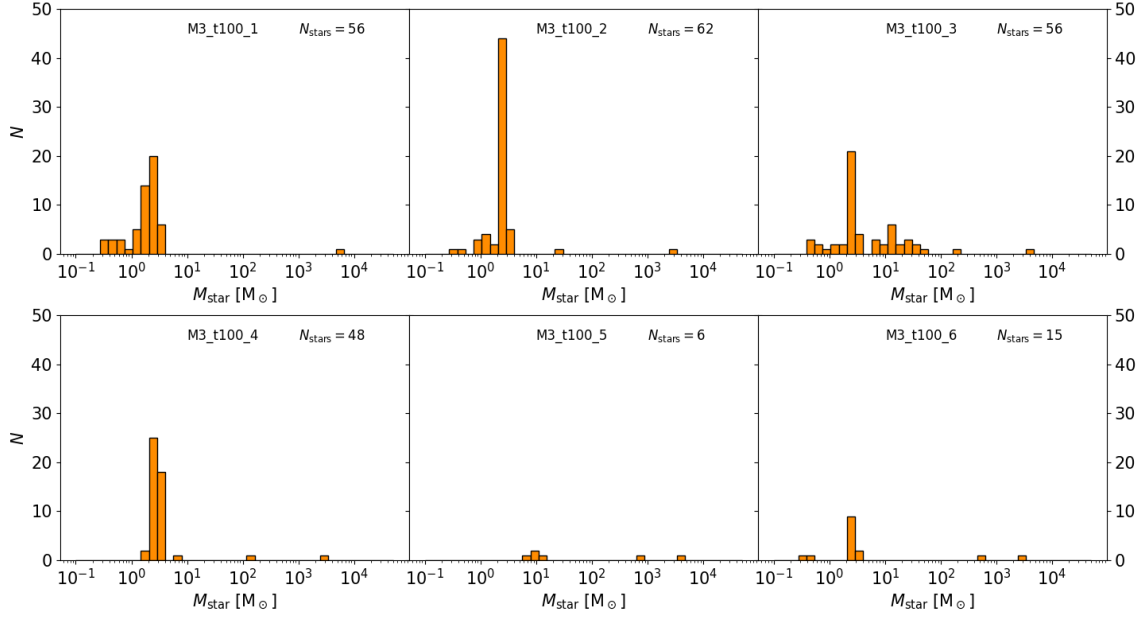


Figure D1. Mass distribution of bound stars at the end of our simulations M1_t100_1–4.

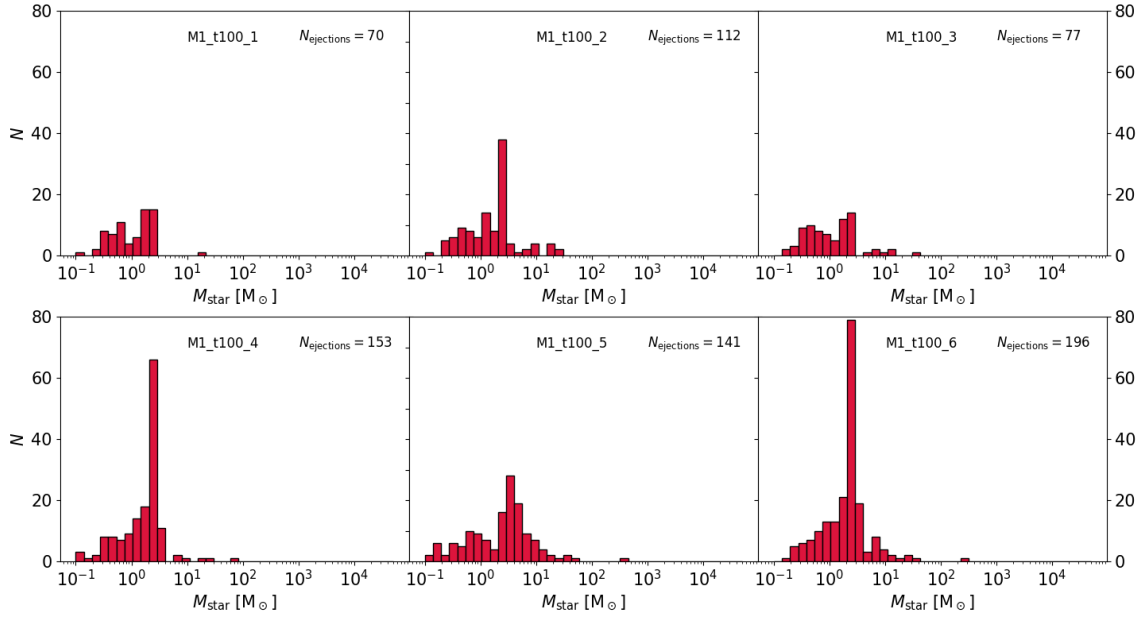


Figure D2. Mass distribution of ejected stars at the end of our simulations M1_t100_1–4.

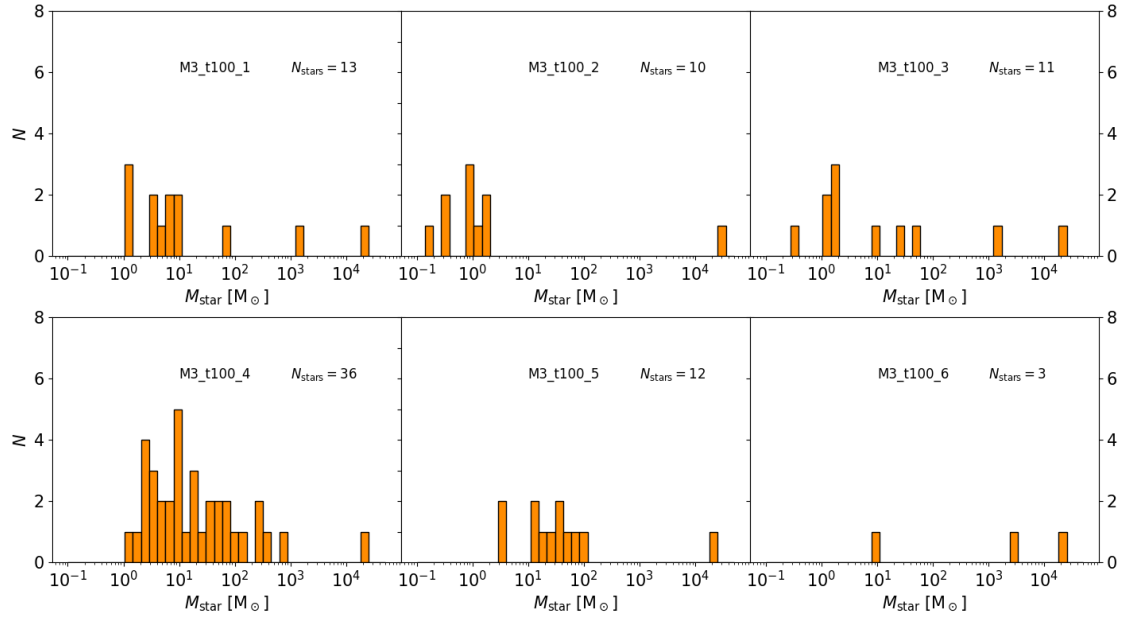


Figure D3. Mass distribution of bound stars at the end of our simulations M3_t100_1–6.

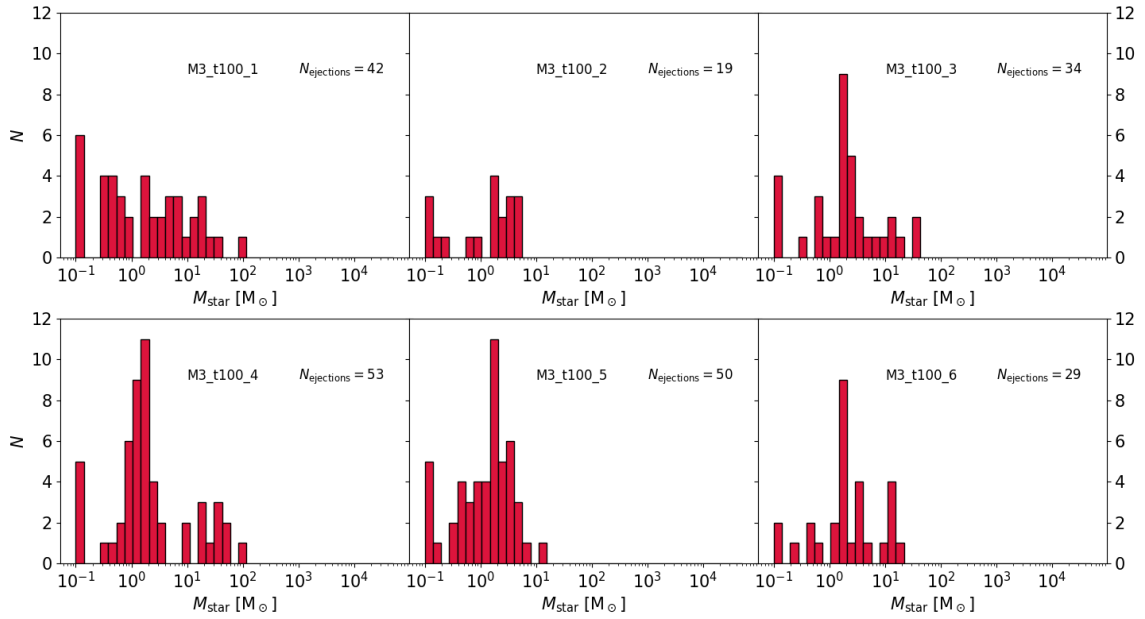


Figure D4. Mass distribution of ejected stars at the end of our simulations M3_t100_1–6.